Please provide feedback

Please support the ScholarWorks@UMBC repository by emailing scholarworks-group@umbc.edu and telling us
what having access to this work means to you and why it's important to you. Thank you.

CrossMark
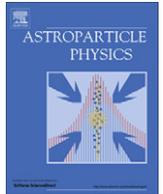
Dark matter and fundamental physics with the Cherenkov Telescope Array

M. Doro [k,*], J. Conrad [h,i,*], D. Emmanoulopoulos [l], M.A. Sànchez-Conde [r,s,t], J.A. Barrio [a], E. Birsin [b], J. Bolmont [c], P. Brun [d], S. Colafrancesco [e,f], S.H. Connell [g], J.L. Contreras [a], M.K. Daniel [j], M. Fornasa [m,n], M. Gaug [k], J.F. Glicenstein [d], A. González-Muñoz [m,n], T. Hassan [a], D. Horns [o], A. Jacholkowska [c], C. Jahn [p], R. Mazini [q], N. Mirabal [a], A. Moralejo [n], E. Moulin [d], D. Nieto [a], J. Ripken [h], H. Sandaker [u], U. Schwanke [b], G. Spengler [b], A. Stamerra [v], A. Viana [d], H.-S. Zechlin [o], S. Zimmer [h], for the CTA Consortium.

[a] Universidad Complutense de Madrid, E-28040 Madrid, Spain
[b] Institut für Physik, Humboldt-Universität zu Berlin, Newtonstr. 15, D 12489 Berlin, Germany
[c] LPNHE, Université Pierre et Marie Curie Paris 6, Université Denis Diderot Paris 7, CNRS/IN2P3, 4 Place Jussieu, F-75252, Paris Cedex 5, France
[d] CEA, Irfu, Centre de Saclay, F-91191 Gif-sur-Yvette, France
[e] School of Physics, University of the Witwatersrand, Johannesburg Wits 2050, South Africa
[f] INAF – Osservatorio Astronomico di Roma, via Frascati 33, I-00040 Monteporzio, Italy
[g] University of Johannesburg, Johannesburg, South Africa
[h] Oskar Klein Centre for Cosmoparticle Physics, Department of Physics, Stockholm University, Albanova, SE-10691 Stockholm, Sweden
[i] K. & A. Wallenberg Research fellow of the Royal Swedish Academy of Sciences, Switzerland
[j] University of Durham, Department of Physics, South Road, Durham DH1 3LE, UK
[k] Universitat Autònoma de Barcelona, Bellaterra, E-08193 Barcelona, Spain
[l] Physics and Astronomy, University of Southampton, SO17 1BJ Southampton, UK
[m] Instituto de Astrofísica de Andalucía (CSIC) & Multidark Fellow, E-18080 Granada, Spain
[n] Institut de Física d'Altes Energies (IFAE), Universitat Autònoma de Barcelona, E-08193 Bellaterra (Barcelona), Spain
[o] Universität Hamburg, Institut für Experimentalphysik, Luruper Chaussee 149, D 22761 Hamburg, Germany
[p] Universität Erlangen-Nürnberg, Physikalisches Institut, Erwin-Rommel-Str. 1, D 91058 Erlangen, Germany
[q] Institute of Physics, Academia Sinica, Taipei 11529, Taiwan
[r] Instituto de Astrofísica de Canarias, E-38205 La Laguna, Tenerife, Spain
[s] Departamento de Astrofísica, Universidad de La Laguna (ULL), E-38205 La Laguna, Tenerife, Spain
[t] SLAC National Laboratory and Kavli Institute for Particle Astrophysics and Cosmology, 2575 Sand Hill Road, Menlo Park, CA 94025, USA
[u] University of Bergen, Bergen, Norway
[v] Department of Physics, University and INFN Siena, I-53100 Siena, Italy

ARTICLE INFO

ABSTRACT

The Cherenkov Telescope Array (CTA) is a project for a next-generation observatory for very high energy (GeV–TeV) ground-based gamma-ray astronomy, currently in its design phase, and foreseen to be operative a few years from now. Several tens of telescopes of 2–3 different sizes, distributed over a large area, will allow for a sensitivity about a factor 10 better than current instruments such as H.E.S.S, MAGIC and VERITAS, an energy coverage from a few tens of GeV to several tens of TeV, and a field of view of up to 10°. In the following study, we investigate the prospects for CTA to study several science questions that can profoundly influence our current knowledge of fundamental physics. Based on conservative assumptions for the performance of the different CTA telescope configurations currently under discussion, we employ a Monte Carlo based approach to evaluate the prospects for detection and characterisation of new physics with the array.

First, we discuss CTA prospects for cold dark matter searches, following different observational strategies: in dwarf satellite galaxies of the Milky Way, which are virtually void of astrophysical background and have a relatively well known dark matter density; in the region close to the Galactic Centre, where the dark matter density is expected to be large while the astrophysical background due to the Galactic Centre can be excluded; and in clusters of galaxies, where the intrinsic flux may be boosted significantly by the large number of halo substructures. The possible search for spatial signatures, facilitated by the larger field of view of CTA, is also discussed. Next we consider searches for axion-like particles which,

* Corresponding author.
  E-mail addresses: doro.michele@gmail.com (M. Doro), conrad@fysik.su.se (J. Conrad).

besides being possible candidates for dark matter may also explain the unexpectedly low absorption by extragalactic background light of gamma-rays from very distant blazars. We establish the axion mass range CTA could probe through observation of long-lasting flares in distant sources. Simulated light-curves of flaring sources are also used to determine the sensitivity to violations of Lorentz invariance by detection of the possible delay between the arrival times of photons at different energies. Finally, we mention searches for other exotic physics with CTA.

1. Introduction

The Cherenkov Telescope Array (CTA) [1] will be an advanced facility for ground-based gamma-ray astronomy in the GeV–TeV regime. Compared to the current generation of Imaging Atmospheric Cherenkov Telescopes (IACT), e.g., H.E.S.S., MAGIC and VERITAS,[1] CTA will feature substantial improvements. It will cover over three decades in energy, from a few tens of GeV up to several tens of TeV. At both ends of this range, interesting new physics is expected, and in addition, a larger energy coverage will provide a bigger lever arm for spectral studies. Above 1 TeV, the field of view (FOV) will be up to 10°, i.e., over a factor of 2 larger than that of current instruments. CTA is currently planned to have a Southern hemisphere site and Northern hemisphere site. This fact together with the large FOV of the telescopes in both installations will likely enable CTA to provide the first extended gamma-ray maps of the sky in the TeV region. The improved energy and angular resolution will enable more precise spectral and morphological observation. This will be achieved by deploying several tens of telescopes of 2–3 different sizes over an area of several square km. CTA will be operated as an open observatory, with improved data dissemination among the world-wide scientific community and a substantial fraction of the total observation time devoted to guest proposals.

The search for new physics beyond the Standard Model (SM) of particle physics is among the key science drivers of CTA along with the understanding of the origin of high-energy gamma-rays and of the physics of cosmic ray acceleration in galactic and extragalactic objects. Several such fundamental physics issues are examined here – the nature of cold dark matter, the possible existence of axion-like particles, and expected violation of Lorentz invariance by quantum gravity effects. Search strategies for cosmic tau neutrinos, magnetic monopoles and follow-up observations of gravitational waves, are also discussed.

The CTA array performance files and analysis algorithms are extensively described in [2]. Eleven array configurations (A...K) were tested for the Southern hemisphere and two (NA, NB) for the Northern hemisphere [2, Table 2]. The simulations were made at an altitude of 2000 m and at 70° elevation. Arrays E and I are considered balanced layouts in terms of performance across the energy range. Arrays A, B, F and G are more focused to low-energies, and arrays C, D and H to high energies. NB is a higher energy alternative to NA. Their point-source sensitivity is compared in [2, Fig. 7]. The arrays comprise different number of telescopes of three different sizes: the Large Size Telescope (LST, 23 m diameter), the Medium Size Telescope (MST, 12 m diameter) and Small Size Telescope (SST, 6 m diameter) [2, Table 1]. One of the goals of this study was to compare different array configurations for the specific scientific case. While in some cases all CTA configurations are compared against each other, in others only benchmarks array B, C and E are considered, as representative arrays that maximize the performance at low-energy, high-energy and in the full-range, respectively. Except for galaxy cluster studies and Galactic halo studies, where extended or diffuse MC simulations are used, in all other cases point-like MC simulations are used. This is the first time that realistic estimates of the prospects of detection for CTA are presented for such searches. An optimised event selection procedure and a dedicated analysis ought to improve on our conservative expectations. Previous studies often relied on too optimistic sensitivities, especially at low energies (<100 GeV); publicly available effective areas for a subset of configurations [1,2] are now accurate and can be used to infer CTA sensitivities for point-like sources.

This contribution is structured as follows:

- In Section 2, we explore different possible scenarios for detection of cold dark matter particle signatures in observations of: dwarf satellite galaxies of the Milky Way (Section 2.1), clusters of galaxies (Section 2.4) and and the Galactic halo (Section 2.8). We also study anisotropies in the diffuse gamma-ray background as a signature of dark matter (Section 2.11).
- In Section 3, we discuss the scientific case for axion-like particles, and make predictions for detection from observation of blazars at different distances and with different flare durations.
- In Section 4, we compare the capacity of all planned CTA arrays to constrain high energy violations of Lorentz invariance, relative to current limits.
- In Section 5 we discuss qualitatively three more cases: the observation of air showers from τ-leptons emerging from the Earth's crust (Section 5.1), the capability to identify magnetic monopoles as bright emitters of Cherenkov light in the atmosphere (Section 5.2) and and some consideration about multi-wavelength gravitational wave campaigns (Section 5.3).

Given the wide variety of physics issues considered in this contribution, an introduction to the individual physics case is presented in each section for easier readability. The reader can find an overall summary and closing remarks in Section 6.

2. Cold dark matter particle searches

A major open question for modern physics is the nature of the dark matter (DM). There is a large body of evidence for the presence of an unknown form of gravitational mass, at scales from kiloparsecs to megaparsecs, that cannot be accounted for by SM particles. The observation by the WMAP satellite [3] of the acoustic oscillations imprinted in the cosmic microwave background quantifies the DM component as contributing about 25% of the total energy budget of the Universe. Being dominant with respect to the baryonic component, which accounts for only about 4% of the total energy density, DM shaped the formation of cosmic structures. By comparing the galaxy distributions in large redshift galaxy surveys [4], and through N-body simulations of structure formation [5–7], it is inferred that the particles constituting the cosmological DM had to be moving non-relativistically at decoupling from thermal equilibrium in the early universe ('freeze-out'), in order to reproduce the observed large-scale structure in the Universe and hence the term "cold DM" (CDM). This observational evidence has led to the establishment of a concordance cosmological model, dubbed ΛCDM [8–10], although this paradigm is troubled by some experimental controversies [11–16].

One of the most popular scenarios for CDM is that of weakly interacting massive particles (WIMPs), which includes a large class

---

[1] Respectively www.mpi-hd.mpg.de/hfm/HESS/, www.magic.mppmu.mpg.de/ and veritas.sao.arizona.edu/.

of non-baryonic candidates with mass typically between a few tens of GeV and few TeV and an annihilation cross-section set by weak interactions (see, e.g., Refs. [17,18]). Natural WIMP candidates are found in proposed extensions of the SM, e.g., in Super-Symmetry (SUSY) [19,20], but also Little Higgs [21], Universal Extra Dimensions [22], and Technicolor models [23,24], among others. Their present velocities are set by the gravitational potential in the Galactic halo at about a thousandth of the speed of light. WIMPs which were in thermal equilibrium in the early Universe would have a relic abundance varying inversely as their velocity-weighted annihilation cross-section (for pure s-wave annihilation): $\Omega_{CDM}h^2 = 3 \times 10^{-27}$ cm^3 s^{-1}/$(\sigma_{ann}v)$ [19]. Hence for a weak-scale cross-section $(\sigma_{ann}v) = 3 \times 10^{-26}$ cm^3 s^{-1}, they naturally have the required relic density $\Omega_{CDM}h^2 = 0.113 \pm 0.004$, where $h = 0.704\pm 0.014$ is the Hubble parameter in units of 100 km s^{-1} Mpcs^{-1} [3]. The ability of WIMPs to naturally yield the DM density from readily computed thermal processes in the early Universe without much fine tuning is sometimes termed the "WIMP miracle".

In some SUSY theories, a symmetry called 'R-parity' prevents a too rapid proton-decay, and as a side-effect, also guarantees the stability of the lightest SUSY particle (LSP), which is thus a prime candidate for a WIMP. WIMPs can annihilate to SM particles, and have hadron or leptons in the final products of annihilation. Thus from cosmic DM annihilations, one can expect emission of neutrinos, charged cosmic rays, multi-frequency electromagnetic radiation from charged products, and prompt gamma-rays [25]. The detection of these final state particles can help to identify DM – this is termed "indirect DM detection". Gamma-rays are not deflected by cosmic magnetic fields, and thus trace back to their origin. Therefore, observation of a gamma-ray signal from cosmic targets where DM is expected could prove conclusive about its nature.

In the context of gamma-ray astronomy, the differential flux of gamma-rays from within a solid angle $\Delta\Omega$ around a given astronomical target where DM is expected, can be written as:

$$\frac{d\Phi(\Delta\Omega, E_\gamma)}{dE_\gamma} = B_F \cdot \frac{1}{4\pi} \underbrace{\frac{(\sigma_{ann}v)}{2m_\chi^2} \sum_i BR_i \frac{dN_\gamma^i}{dE_\gamma}}_{\text{Particle physics}} \cdot \underbrace{\tilde{J}(\Delta\Omega)}_{\text{Astrophysics}}, \qquad (1.1)$$

where $(\sigma_{ann}v)$ is the annihilation cross-section (times the relative velocity of the two WIMPs), $\sum_i BR_i dN_\gamma^i/dE_\gamma = dN_\gamma/dE_\gamma$ is the photon flux per annihilation summed over all the possible annihilation channels i with branching ratios BR_i, and m_χ is the mass of the DM particle. The 'astrophysical factor' $\tilde{J}$ is the integral over the line of sight (los) of the squared DM density and over the integration solid angle $\Delta\Omega$:

$$\tilde{J} = \int_{\Delta\Omega} d\Omega \int_{los} ds\, \rho^2(s, \Omega). \qquad (1.2)$$

The remaining term B_F in Eq. (1.1) is the so-called 'boost factor' which is a measure of our ignorance of intrinsic flux contributions that are not accounted for directly in the formula.

There are various known mechanisms for boosting the intrinsic flux, among which we mention the inclusion of subhalos, and the existence of a 'Sommerfeld enhancement' of the cross-section at low velocity regimes in models where the DM particles interact via a new long-range force. All numerical N-body simulations of galactic halos have shown the presence of subhalos populating the host halo (see, e.g., Refs. [5,26]). Such density enhancements, if not spatially resolved, can contribute substantially to the expected gamma-ray flux from a given object. This effect is strongly dependent on the target: in dwarf spheroidal galaxies (dSphs) for example the boost factor is only of $\mathcal{O}(1)$ [27,28], whereas in galaxy clusters the boost can be spectacular, by up to a factor of several hundreds [29–31]. On the other hand, the Sommerfeld enhancement effect can significantly boost the DM annihilation cross-sec-

tion [32,33]. This non-relativistic effect arises when two DM particles interact in a long-range attractive potential, and results in a boost in gamma-ray flux which increases with decreasing relative velocity down to a saturation point which depends on the DM and mediator particle mass. This effect can enhance the annihilation cross-section by a few orders of magnitude [27,28].

The current generation of IACTs is actively searching for WIMP annihilation signals. dSphs are promising targets for DM annihilation detection being among the most DM dominated objects known and free from astrophysical background. Constraints on WIMP annihilation signals from dSphs have been reported towards Sagittarius, Canis Major, Sculptor and Carina by H.E.S.S. [34,35,28], towards Draco, Willman 1 and Segue 1 by MAGIC [36–38], towards Draco, Ursa Minor, Boötes 1, Willman 1 and Segue 1 by VERITAS [39,40], and again towards Draco and Ursa Minor by Whipple [41]. Nevertheless, the present instruments do not have the required sensitivity to reach the "thermal" value of the annihilation cross-section $(\sigma_{ann}v) = 3 \times 10^{-26}$ cm^3 s^{-1}. A search for a WIMP annihilation signal from the halo at angular distances between 0.3° and 1.0° from the Galactic Centre has also recently been performed using 112 h of H.E.S.S. data [42]. For WIMP masses well above the H.E.S.S. energy threshold of 100 GeV, this analysis provides the currently most constraining limits on $(\sigma_{ann}v)$ at the level of a few $\times 10^{-25}$ cm^3 s^{-1}. H.E.S.S., MAGIC and VERITAS have also observed some galaxy clusters, reporting detection of individual galaxies in the cluster, but only upper limits on any CR and DM associated emission [43–48]. Even though IACT limits are weaker than those obtained from the Fermi-LAT satellite measurements in the GeV mass range [49–52], they complement the latter in the TeV mass range. Gamma-ray line signatures can also be expected in the annihilation or decay of DM particles in space, e.g., into $\gamma\gamma$ or $Z^0\gamma$. Such a signal would be readily distinguishable from astrophysical gamma-ray sources which typically produce continuous spectra [53]. A measurement carried out by H.E.S.S. Spengler et al. [54] using over 100 h of Galactic Centre observations and over 1000 h of extragalactic observations complements recent results obtained by Fermi-LAT [55], and together cover about 3 orders of magnitude in energy, from 10 GeV to 10 TeV.

In this contribution, we focus on the prospects for DM searches with CTA, which are expected to improve on the current generation of IACTs on the following basis:

- the energy range will be extended, from a few tens of GeV to several tens of TeV. At low energies, this will allow overlap with the Fermi-LAT instrument, and will provide sensitivity to WIMPs with low masses. For WIMPs with mass larger than about 100 GeV, CTA will have higher sensitivity as our studies indicate [56].
- the improved sensitivity in the entire energy range, compared to current instruments, will obviously improve the probability of detection, or even *identification* of DM, through the observation of spectral features,
- the increased FOV (about 10 deg versus $2 - 5$ deg) with a much more homogeneous sensitivity, as well as the improved angular resolution, will allow for much more efficient searches for extended sources like galaxy clusters (Section 2.4) and and spatial anisotropies (Section 2.11),
- finally, the improved energy resolution will allow much better sensitivity to the possible spectral feature in the DM-generated photon spectrum. While astrophysical sources show typically power-law spectra with steepening at high energies, DM spectra are universal and generically exhibit a rapid cut-off at the DM mass. For specific models, "smoking gun" spectral features can appear [53]. The observation of a few identical such spectra from different sources will allow both precision determination of the mass of the WIMP and its annihilation cross-section.

For the following studies, in order to have a detection, we require (a) the number of excess events over the background larger than 10 in the signal region, (b) the ratio between the number of excess events and the background events larger than 3%, and (c) the significance of the detection computed following Eq. (17) of Li and Ma [57], to be larger than 5. If not explicitly mentioned, we used a number of background-control regions set to 5 ($\alpha = 0.2$ in the Li and Ma notation), which is a conservative choice, given the fact that the large FOV of CTA may allow for $\alpha < 0.2$. In case of non detection within a certain observation time, we calculate integral upper limits following the methods described in [58] (bounded profile likelihood ratio statistic with Gaussian background, and with a confidence level of 95% C.L) in all cases expect the Galactic halo case, where we use the method of [59].

We study the effect of various annihilation spectra, assuming in turn 100% BR into a specific channel ($b\bar{b}, \tau^+\tau^-$ or $\mu^+\mu^-$). The spectral shapes are obtained from different parameterisation from the literature [60–62]. For the $b\bar{b}$ channel, which is used for comparison of different targets (see Fig. 23), this difference accounts for few percents (depending on the DM mass), which is substantially smaller than the uncertainties in, e.g., the astrophysical factor, and do not significantly alters the conclusions.

2.1. Observations of dwarf satellite galaxies

In the ΛCDM paradigm, galaxies such as ours are the result of a complex merger history and are expected to have extended halos of DM in accordance with observations. dSphs are satellites orbiting the Milky Way under its gravitational influence and are considered as privileged targets for DM searches for the following reasons:

- the study of stellar dynamics shows that dSphs are among the most DM-dominated systems in the Universe, with mass-to-light ratio up to a few hundreds. In particular, the otherwise very uncertain astrophysical factor (Eq. (1.2)) can be constrained by dynamical arguments [63],
- many of the dSphs lie within ∼100 kpc of the Earth,
- they have favourable low gamma-ray backgrounds due to the lack of recent star formation history and little or no gas to serve as target material for cosmic-rays [64].

The family of dSphs is divided into "classical" dSphs, which are well-established sources with relatively high surface brightness and hundreds of member stars identified [65,66], and "ultra-faint" dSphs, which have mainly been discovered recently through photometric observations in the Sloan Digital Sky Survey (SDSS) [67] and have very low surface brightness and only a few tens or hundreds of member stars. Some of the ultra-faint dSphs are not well-established as such because of similarity of their properties with globular clusters, hence their nature is often under debate. However, they are of particular interest due to their potentially very large, albeit uncertain, mass-to-light ratios.

Table 1.1 shows the astrophysical factor $\tilde{J}$ for few selected dSphs for comparison. For the classical dSphs, we selected the two most promising Northern (Ursa Minor and Draco) and Southern (Sculptor and Carina) ones according to [66, Table 2]. The statistical uncertainties on the astrophysical factor are roughly one order of magnitude at 68% CL, slightly depending on the dSphs, and can be found in [66, Table 2]. For the ultra-faint dSphs, we include Segue 1, Willman 1 and Coma Berenices, which have the highest $\tilde{J}$-values (although their nature is still under debate, especially for Segue 1 [70–76], which makes the determination of the astrophysical factor less accurate than for classical dSphs). We remark how the estimation of the astrophysical factor is subject to

Table 1.1
Astrophysical factors for a selection of the most promising classical and ultra-faint dSphs. Dec. is the target declination, D the distance and $\tilde{J}$ is defined as in Eq. (1.2).

dSph	Dec. (deg)	D (kpc)	$\tilde{J}$ (GeV^2 cm^{-5})	Profile	Ref.
Ursa minor	+44.8	66	2.2×10^{18}	NFW	[66]
Draco	+34.7	87	7.1×10^{17}	NFW	[66]
Sculptor	−83.2	79	8.9×10^{17}	NFW	[66]
			2.7×10^{17}	ISO	[68]
Carina	−22.2	101	2.8×10^{17}	NFW	[66]
Segue 1	+16.1	23	1.7×10^{19}	Einasto	[38]
Willman 1	+51.1	38	8.4×10^{18}	NFW	[39]
Coma Berenices	+23.6	44	3.9×10^{18}	NFW	[69]

uncertainties of either statistical origin or due to the different assumptions considered for its calculation. A systematic study has been done for Sculptor, to estimate the effect of the profile shape and velocity anisotropy assumptions [68]. Another compilation of astrophysical factors for several dSphs can be found in [52].

For the subsequent discussion, we consider only three sources: Ursa Minor and Sculptor representative of classic dSphs and located in the Northern and Southern hemisphere respectively, and Segue 1 having the largest astrophysical factor.

2.2. Bounds on the annihilation cross-section

Two kinds of radial profiles are generally used to model the DM distribution in dSphs: *cusped* and *cored* profiles [77]. While the former is motivated by numerical *N*-body simulations, the latter seems to be more consistent with observations [78], but the issue is still under debate (see, e.g., [79]). The standard cusped profile is the Navarro, Frenk and White form (NFW) [80], while more recently it has been shown that the Einasto profile [81] provides also a good fit to the subhalos in *N*-body simulations [5]. On the other hand, for systems of the size of dSphs, the possibility of centrally cored profiles has also been suggested [82,83,14]. In conclusion, observations of low surface brightness and dSphs [84–86] show that both cusped and cored profiles can accommodate their stellar dynamics.

Fig. 1 shows the integral upper limits towards Sculptor, the best Southern candidate from Table 1.1, for which we consider both a cusped NFW [66] and a cored isothermal [28] profile. The sensitivity is calculated assuming that the DM particle annihilates purely in the $b\bar{b}$ channel, for arrays B, C and E. The observation time is set to 100 h and the integration solid angle to $\Delta\Omega = 10^{-5}$ sr. The best reached sensitivity is at the order of few $\times 10^{-23}$ cm^3 ss^{-1} for the NFW profile for both arrays *E* and *B*, while the isothermal profile is less constraining. Weaker constraints in the low mass range are obtained for the *C* array due to the lack of the large-size telescopes in the centre of their layout. The capability of CTA to discriminate between the two profiles is therefore restricted.

The integration solid angle plays a central role in the estimation of the sensitivity and in the discrimination of the cusp or core profiles. The former point was addressed already [66, Fig. 7] where it was shown that small integration angles guarantee the strongest constraints. In the case of CTA, depending on the array layout (and the energy range), the angular resolution could be as low as $0.02°$, corresponding to a minimum integration angle of about 10^{-6} sr, and thus our results can be considered conservative, with an expected improvement of up to a factor ~ 2. Concerning the second point, [87] showed that the more robust constraints, regardless of whether the profile is cored or cusped, are reached for an integration angle $r_c = 2r_{1/2}/D$, where $r_{1/2}$ is the so-called half-light radius, and D is the distance to the dSph. For Sculptor, $r_c = 0.52$, which is over 5 times the integration angle adopted here.
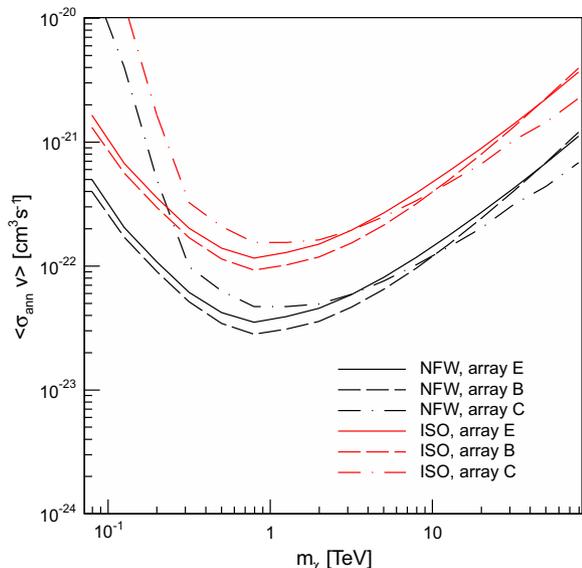
Fig. 1. CTA sensitivities on the velocity-averaged annihilation cross-section as a function of the WIMP mass for 100 h observation of Sculptor with the CTA array E (solid line), B (dashed line) and C (dashed-dotted line). Both the NFW (black line) and cored isothermal (ISO, red line) DM halo profiles are shown, for an integration solid angle $\Delta\Omega = 1 \times 10^{-5}$ sr. Annihilations are assumed to occur with 100% branching ratio into $b\bar{b}$. (For interpretation of the references to colour in this figure legend, the reader is referred to the web version of this article.)

In our calculation this would imply a weakening of the upper limits of a factor of a few.

In Fig. 2 we show the integral upper limits for two classical dSphs, namely Ursa Minor and Sculptor in the Northern and Southern hemispheres respectively, as well as the ultra-faint dSph Segue 1. In order to span the variety of DM particle models, we study the effect of various annihilation spectra (computed using Ref. [61], assuming in turn 100% BR into $b\bar{b}, \tau^+\tau^-$ and $\mu^+\mu^-$ channels for the array E and an observation time $T_{obs} = 100$ h. Assuming the annihilation to be purely into $\tau^+\tau^-$, the sensitivity reaches few $\times 10^{-25}$ cm^3 ss^{-1} for 100 h observation time of Segue 1. In
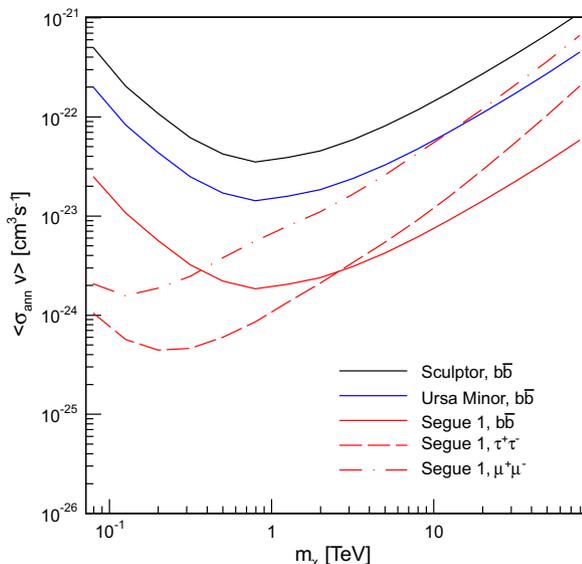
comparing the different dSphs (assuming the reference annihilation channel $b\bar{b}$) we see that even the most promising classical dSphs are less constraining than Segue 1 by over a factor of 10. However the uncertainties in the estimation of astrophysical factors for ultra-faint dSphs mean that this conclusion may not be reliable. Note that in the above calculations we did not assume any intrinsic flux boost factor, i.e., $B_F = 1$ in Eq. (1.1).

2.3. Bounds on astrophysical factors and boost factors

Another approach to estimate the capabilities of CTA for DM detection in dSphs consists in the evaluation of the statistical significance of the DM signal as a function of the DM particle mass m_χ and the astrophysical factor, for different possible annihilation channels. Hereafter, we calculate the minimum astrophysical factor J_{min} required to reach a statistical significance of 5σ assuming an effective observation time of 100 h, and the thermal cross-section 3×10^{-26} cm^3 s^{-1}. This is shown in Fig. 3 for two annihilation channels: $b\bar{b}$ (upper curves) and $\tau^+\tau^-$ (lower curves), using analytical fits from Ref. [88]. Again, three proposed CTA configurations are studied: B, C, and E. In order to put these values into context, we note that the largest astrophysical factor $\bar{J}$ for known dSphs is that of Segue 1 at 1.7×10^{19} GeV^2 cm^{-5} [89]. From the figure we see that array B is the most constraining over the whole energy range. It is clear that for a detection, the astrophysical factor of the dSph needs to exceed 10^{21} GeV^2 cm^{-5}, which is only 1–2 orders of magnitude smaller than that of the Galactic Centre (see Section 2.8). While we may expect a few such objects in the Milky Way halo [90], they ought to have already been detected and identified by Fermi-LAT. Although this has not happened, one can envisage DM subhalos with no associated dSph (or one not bright enough optically to be detected), and therefore such gamma-ray emitters may be hidden among the unidentified Fermi sources [91].

Another way to evaluate the prospects of DM detection is by means of the intrinsic flux *boost factor* term B_F in Eq. (1.1). The minimum B_F is computed as the ratio of the minimum astrophysical factor J_{min} which provides a 5σ detection in 100 h of observation time with CTA, to the observational astrophysical factor $\bar{J}$ from

Fig. 2. CTA sensitivities on the velocity-averaged annihilation cross-section versus the WIMP mass for 100 h observation towards Sculptor, Ursa Minor and Segue 1, assuming 100% branching ratio into $b\bar{b}$ (for Segue 1 also into $\tau^+\tau^-$ and $\mu^+\mu^-$). The calculations are done for array E and $\Delta\Omega = 1 \times 10^{-5}$ sr.
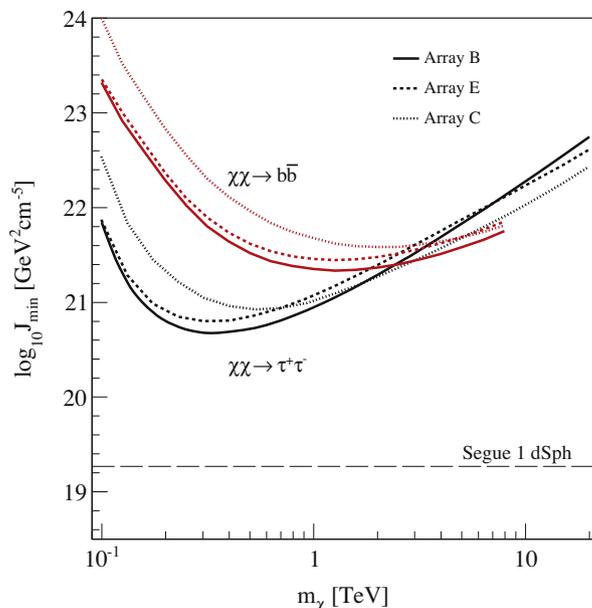

Fig. 3. The minimum value of the astrophysical factor required for a 5σ detection with $T_{obs} = 100$ h, versus WIMP mass. Two annihilation channels are considered for arrays B, C, and E: $b\bar{b}$ (upper curves) and $\tau^+\tau^-$ (lower curves). The estimated astrophysical factor for Segue 1 is shown for comparison.
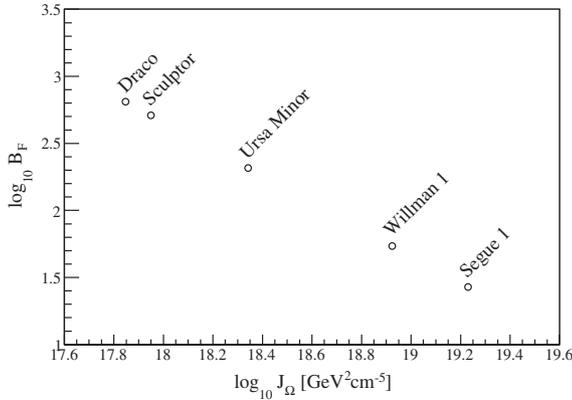
Fig. 4. Minimum boost factor required for a 5σ detection in 100 h by array B, for the dSphs in Table 1.1 and a 1 TeV WIMP annihilating into $\tau^+\tau^-$. The density profiles are taken to be NFW, except for Segue 1 where an Einasto profile has been assumed. The smallest boost required is $B_F = 25$ for Segue 1.

the DM modeling of the dSphs. Again, the thermal cross-section 3×10^{-26} cm^3 s^{-1} is assumed. Fig. 4 shows the minimum B_F for a 1 TeV DM particle annihilating into $\tau^+\tau^-$. J_{obs} is calculated for a NFW profile for all the cases except Segue 1, where an Einasto profile is considered. Considering that the boost factor from subhalos in dSph is only of $\mathcal{O}(1)$, CTA observations of dSphs will be more sensitive to scenarios where Sommerfeld enhancement is at play, which may instead boost the signal up to $\mathcal{O}(1000)$.

2.4. Observations of galaxy clusters

Within the standard ΛCDM scenario, galaxy clusters, with masses around $10^{14} - 10^{15}$ M$_\odot$, are the largest gravitationally bound objects and the most recent structures to form [92]. They are complex objects, relevant for both cosmological and astrophysical studies, and for what concerns DM searches [25,29,30,93–100]. DM, in fact, is supposed to be the dominant component of the cluster mass budget, accounting for up to 80% of its mass (the other components are the galaxies and the gas of the intra-cluster medium (ICM)). This is why clusters have been considered as targets for the indirect detection of DM, with the possibility of detecting the gamma-rays produced in the annihilation (or decay) of DM particles in the halo of the cluster.

N-body simulations of halo formation and evolution have also proven that, while the majority of early-formed, small structures merge together giving shape to more massive objects, some of the subhalos survive and are still present in the "host" halo of larger objects. Theoretical models foresee a huge number of these substructures at all scales down to $10^{-11} - 10^{-3}$ M$_\odot$ [101]. These subhalos have the effect of contributing to the total gamma-ray emission from DM annihilations, and they may have important consequences for DM indirect detection. This is especially true for galaxy clusters, where the intrinsic flux "boost" from subhalos can be of order $100 - 1000$, in particular compared to the case of dSphs, explored previously, where the subhalos boost should contribute only marginally. Despite the fact that, due to their vicinity, dSphs are usually considered as the best sources for DM indirect detection, thanks to the subhalos boost, some authors claim that galaxy clusters have prospects of DM detection better or at least as good as those of dSphs [29–31].

On the other hand, in galaxy clusters, emission in the gamma-ray range is not only expected by DM annihilation. Clusters may host an Active Galaxy Nucleus (AGN, that appear as point-like sources at very high energies) and radio galaxies. The case of the Perseus galaxy cluster, which has been observed by MAGIC during

several campaigns in the last years, is emblematic: MAGIC detected both the central AGN NGC-1275 [102] and the off-centreed head–tail radio galaxy IC 310 [103]. Moreover gamma-rays are expected to be produced also from the interaction of cosmic rays (CRs) with the ICM [95,104–107]. The physics of the acceleration of CRs (electrons and protons) is not completely understood, but plausible mechanisms can be shock acceleration during structure formation, or galactic winds driven by supernovae. CRs can also be injected into the ICM from radio galaxy jets/lobes. At the energies of interest here (above 10 GeV), CRs emit gamma-rays from the processes associated with the decay of the neutral and charged pions produced in the interaction of the CRs with the ICM ambient protons [108,109]. Most importantly, such a contribution is usually found to be larger than the one predicted from DM annihilation. It thus represents an unavoidable source of background for DM searches in galaxy clusters. To date, the deep exposure performed with the MAGIC stereoscopic system of the Perseus cluster [47] placed the most stringent constraints from VHE gamma-rays observations regarding the maximum CRs-to-thermal pressure to $\langle X_{CR} \rangle < 1 - 2\%$.

The purpose of this section is to estimate the CTA potential to detect gamma-rays from DM annihilation in the halo of galaxy clusters. First, the CR-induced emission only will be considered. This component represents, by itself, an extremely interesting scientific case, at the same time being a background complicating the prospects of DM detection. Afterward, the ideal case of a cluster whose emission is dominated by DM annihilation only will be treated. Finally, the combination of the two components distributed co-spatially will be discussed.

It should be noted here that gamma-ray emission from both DM annihilation and CRs is spatially extended, even though not always co-spatial. In particular, [29] proved that, for the case of DM, the contribution of subhalos is particularly relevant away from the halo centre, so that annihilations can still produce a significant amount of photons up to a distance of $1 - 2$ degrees from the centre. This represents a problem for current Cherenkov Telescopes since their FOV is limited to 3–5°. CTA will overcome this limitation, having a FOV of up to 10° (at least above 1 TeV) and an almost flat sensitivity up to several degrees from the centre. It is reasonable to expect, therefore, that CTA will allow a step-change in capability in this important area.

In this study, we selected two benchmark galaxy clusters: Perseus and Fornax. Perseus has been chosen because it is considered that with the highest CR-induced photon yield but a low DM content, and Fornax for the opposite reason: it is considered the most promising galaxy cluster for DM searches [29,30]. We recall that Perseus is located in the Northern hemisphere, while Fornax is in the Southern hemisphere. To study the prospects for CTA we use two Monte Carlo simulations of the instrument response functions and of the background rates for *extended sources*, for the case of array B and array E, which we recall, are representatives of well-performing arrays at low energies (array B) and in the full energy range (array E). The MC simulations were developed explicitly for the analysis of extended sources so that all the relevant observables are computed throughout the entire FOV.

2.5. Gamma-ray emission from cosmic-rays

Gamma-ray emission due to the injection of CRs into the ICM of a galaxy cluster is proportional both to the density of the ICM and the density of CRs. For the present work, we refer to the hadronic CR model of Pinzke and collaborators [30,95], based on detailed hydrodynamic, high-resolution simulations of the evolution of galaxy clusters, since in these works we found detailed morphological information, essential to compute the CTA response. The CR surface brightness rapidly decreases with the distance from the centre of the halo, so that, in most cases, the total emission is contained in

$0.2 - 0.3\,r_{200}$, where r_{200} is the projected virial radius of the cluster, where the local density equals 200 times the critical density (see, e.g., Fig. 14 of [30], from which we derive the surface brightness of the clusters we analyze). $r_{200} = 1.9$ Mpc ($1.4°$) for Perseus and 0.96 Mpc ($2.8°$) for Fornax [29]. The energy spectrum of the model, in the energies of interests here (above 10 GeV), is a power-law with a slope of -2.25.

Since the emission region is extended in the sky, we first divide the FOV into a grid of pixels each 0.2 degrees wide, and then we define the region of interest (ROI), constituted by all the pixels within an angle θ_{max} from the centre of the camera. We consider 15 values of energy threshold E_i in logarithmic steps from 50 GeV to 50 TeV. With the theoretical gamma-ray emission and the instrument response, we are able to compute the predicted number of background (N_i^{OFF}) and signal events (N_i) above each E_i, in each bin of the ROI separately, and then we integrate over the entire ROI. The model of [30] predicts a rather large gamma-ray flux for Perseus ($\Phi_{CR}(>100\ \text{GeV}) = 2.04 \times 10^{-11}\ \text{cm}^{-2}\ \text{s}^{-1}$), the largest among the galaxy clusters, and a smaller one for Fornax ($\Phi_{CR}(>100\ \text{GeV}) = 1.5 \times 10^{-13}\ \text{cm}^{-2}\ \text{s}^{-1}$). Above the different energy thresholds E_i, we determine how many hours CTA will need to detect the sources. We perform the calculation for the two CTA array B and E and for different ROI. We repeat the procedure 10 times for each energy threshold and average the results, in order to quantify the statistical fluctuations occurring when the number of events (both N_i and N_i^{OFF}) are generated. The results are shown in Fig. 5.

If one assumes the CR-induced gamma-ray model by [30], CTA will detect such radiation from Perseus already in about 100 h, a fact which will constitute an extraordinary scientific result by itself.[2] The discovery could indeed be potentially close, opening up a completely new observation window on the Universe. We underline that there is an absolute lower limit for gamma-rays in the hadronic scenario for clusters with an observed radio halo: a stationary distribution of CR electrons loses all its energy to synchrotron radiation for strong magnetic fields, as those in the radio halo, and therefore the ratio of gamma-ray to synchrotron flux becomes independent of the spatial distribution of the CRs and the thermal gas. For the Perseus cluster this lower limit is roughly a factor 3–4 from the gamma-ray flux predicted by the CR model (see Fig. 3 in Ref. [47]), hence CTA would, in the worst case scenario, require about $1,000$ hours of observation to completely rule out the hadronic models. Such large observation times can in principle be achieved either by, e.g., multi-annual observational campaigns. On the other hand, a non detection with CTA in a few hundred hours would seriously constrain the model and thus pose interesting challenges on the galaxy cluster physics. The situation is more pessimistic for our model of Fornax, which is out of reach for CTA.

We see that the exact value of the integration time depends on the energy threshold chosen for the analysis. The reason for this is the tradeoff between the gamma-ray efficiency at different energies (the effective area), the source intrinsic spectrum and the chosen ROI. Roughly 90% of the CR-induced emission is expected within about $0.1\,r_{200}$ for Perseus, which corresponds to roughly $0.2°$. We checked that integrating larger ROI, more background than signal is included in the analysis, thus deteriorating the significance of the detection. This suggests that in realistic cases, the best ROI should be optimized. Finally, we also see that the prospects of detection are similar for both considered arrays, B and E.
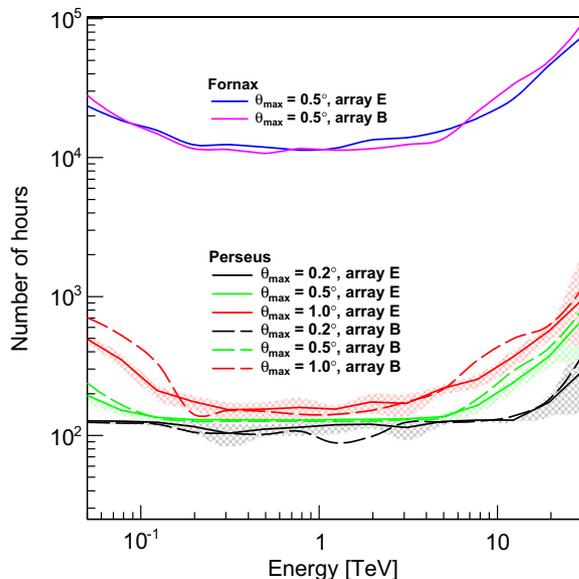

Fig. 5. Integration time required to have a 5σ detection (see text for details) of gamma-rays from CR-induced gamma-rays only according to the model of [30] for Perseus (lower curves, $\Phi_{CR}(> 100\ \text{GeV}) = 2.04 \times 10^{-11}\ \text{cm}^{-2}\ \text{s}^{-1}$) and Fornax (upper curves, $\Phi_{CR}(> 100\ \text{GeV}) = 1.5 \times 10^{-13}\ \text{cm}^{-2}\ \text{s}^{-1}$). The integration time is shown as a function of the energy threshold, and over different ROI, for the case of array B (dashed lines) and array E (solid lines). The shaded regions indicate the 1σ standard deviation among 10 different simulations.

2.6. Gamma-ray emission from dark matter annihilation

The gamma-ray brightness due to DM annihilations from a particular viewing angle in the sky is proportional to the DM density squared integrated along the line of sight, as shown in Eq. (1.1). In the case of galaxy clusters, the contribution of the smooth DM halo is boosted by the presence of DM subhalos. Recent N-body simulations of Milky Way-like halos [5–7] found that the contribution of subhalos is small in the centre of the halo, due to dynamical friction and tidal effects that disrupt the subhalos. However, already at distances of $0.01 - 0.05\,r_{200}$, subhalos become the dominant component. The real value of the boost factor from subhalos is unknown and the theoretical estimates depend on different assumptions and different methods used in the calculations. [30] estimated a $B_F = 580$ and 910 for Fornax and Perseus respectively (for a minimal halo mass of $10^{-6}\ M_\odot$), while other authors gave B_F from few tens [29] up to several thousands [31].

We refer again to the results of [30] where the authors assumed a double power-law to describe the luminosity of subhalos as a function of the projected distance from the centre of the halo, a behavior derived by analyzing the sub-halos in the Aquarius N-body simulation. They also found the projected surface brightness to be largely independent of the initial profile of the smooth DM halo. As a result, the DM profile is very flat since the emission decreases approximately only 10% at a distance of $1.5 - 2.0$ degrees from the centre, depending on the cluster [Fig. 7 and Ref. [29]]. For the case of Perseus and Fornax, we used the results of Fig. 10 of Ref. [30], assuming a telescope angular resolution of 0.1 degree, which is a good approximation for CTA, despite the fact that the exact value depends on the array, the energy and the position in the FOV. We underline that in the case of galaxy cluster, the contribution from substructure strongly shapes the region of emission, basically moving from a point-like source (in case no substructure are considered), to an extended source. Given the fact that the analysis differ in the two cases, the contribution from substructure cannot be considered as a simple multiplicative factor in the intrinsic expected flux with respect to point-like case.
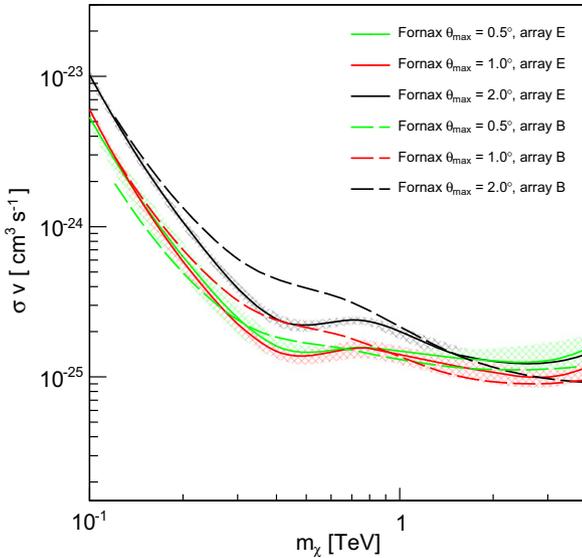
Fig. 6. Prospect of detection of DM-induced signal from Fornax for a DM particle annihilating into $b\bar{b}$ and 100 h integration time. The reference model is taken from Ref. [30] with subhalo boost factor $B_F = 580$. The shaded regions indicate the 1σ standard deviation among 10 different simulations.

Hereafter we consider the Fornax cluster, which has the largest expected DM-induced photon yield. The intrinsic flux is taken from [30, Table 2] and includes an intrinsic boost factor from subhalos of $B_F = 580$, summing up to a total flux of $\Phi_{DM}(>100 \text{ GeV}) = 3.6 \times 10^{-13} \text{ cm}^{-2} \text{ s}^{-1}$. Additional intrinsic boost factor may come from either other contributions from subhalos not accounted in this model, by mechanisms like the Sommerfeld enhancement discussed above, or by the effect of contraction processes due to baryonic condensation [110,111].

To compute the CTA prospects of detection, we consider only the case of DM annihilating into $b\bar{b}$ (spectral shape obtained from Ref. [88], while other channels like $\tau^+\tau^-$ or $\mu^+\mu^-$ may be more constraining, depending on the energy (see Fig. 2). We take the reference thermal cross-section $3 \times 10^{-26} \text{ cm}^3 \text{ s}^{-1}$ and we scan DM particle mass m_χ between 50 GeV and 4 TeV. We optimized the upper limit calculation as described in Ref. [38], by optimizing the energy threshold above which the upper limit is estimated. In addition, we consider the possibility of extending the size of the ROI up to a θ_{max} of 2 degrees, to encompass the full radial extension of the source. Fig. 6 show the results. In 100 h observation, the lack of detection would place exclusion limits at the level of $10^{-25} \text{ cm}^3 \text{ s}^{-1}$.

We also studied the effect of integrating over larger and larger regions: despite the increased numbers of background events, the signal yield is also larger and, in the case of Fornax, we gain more in integrating up to $\theta_{max} = 1°$ than $0.5°$, while integrating over larger regions leads to a worse sensitivity.

2.7. Distinguishing the dark matter signal from other gamma-ray contributions

In the previous sections we have considered separately the contributions of CR and DM to the total gamma-ray photon yield. This is an unrealistic situation: galaxy clusters are, in fact, complex objects where gamma-rays may be due to different contributions possibly of different spatial origin: by collisions of accelerated CRs, by DM annihilations *and* by foreground or embedded astrophysical sources.

Fortunately, gamma-rays of different origin typically have different spectral shapes, with the DM-induced emission characterized by the peculiar cut-off at $E = m_\chi$ and other remarkable spectral features [113,112], in contrast to the plain spectral shapes (typically power-laws within the energy range of interest here) of the emission due to CRs, of the central galaxy or any astrophysical objects in the cluster. In the case a VHE emission is detected from a cluster, this fact may be used as a probe to discriminate between the components. However, we remark that in order to significantly discriminate the two sources one would need a quite significant detection over the CR-signal, which is often not supported by theoretical predictions for most galaxy clusters.

A distinct approach could be based on the different spatial extensions of the various contributions of VHE gamma-ray photons from galaxy clusters. The possible individual galaxies emitting within the cluster are typically seen as point-like sources, and thus one may exclude them from the FOV for CR and DM searches. Moreover, from the fact that CR-induced radiation is more concentrated than that induced by DM, one can optimize the ROI to select only those where the emission is DM dominated. In Fig. 7, we show the expected brightness profile for CR and DM photons for the Fornax cluster. One can see that up to $\theta = 0.4°$ the emission is dominated by CR-induced photons, whereas this exact value is cluster-dependent and model-dependent, and in particular the possible intrinsic boost-factor in the DM signal can affect this. In this example, above $\theta = 0.4°$, the CR-signal fades more rapidly than the DM one. Then, in principle, by considering a ROI with a $\theta_{min} = 0.4°$, one could be able to isolate the DM signal. The maximum integration angle θ_{max} should be optimized according to the specific cluster and emission profile to maximize the sensitivity, as discussed above. Unfortunately, at the moment of writing this report, we did not have sufficient coverage in the MC of extended sources to perform such a study, and we are limited to a qualitative discussion. We mention that the "geometrical" discrimination makes sense only if the DM signal is sufficiently large, otherwise different observational strategies could be more constraining. Finally, we stress again that with a large FOV (at least above 1 TeV) that has a near constant sensitivity over several degrees will allow CTA to study extended high energy gamma-ray sources in detail for the first time, with possibly revolutionary consequences for the IACT technique.
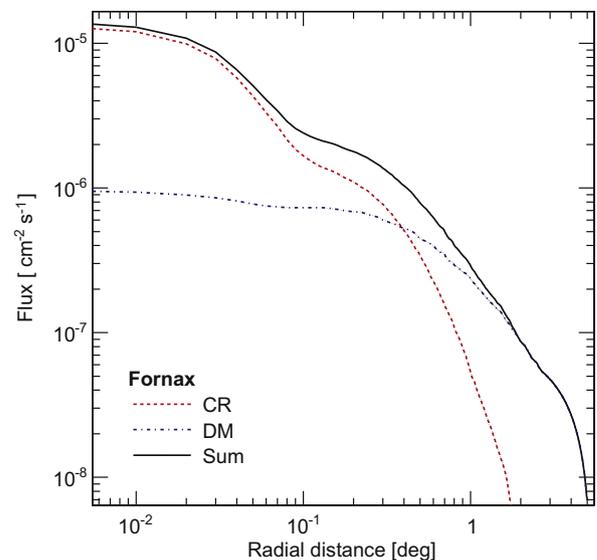

Fig. 7. The surface brightness (above 1 GeV) of the gamma-ray emission from the Fornax cluste from CRs (red), DM (blue) and the sum of the two contributions (black). The DM emission is calculated from the K' benchmark model of [112] which has mass of 570 GeV and a velocity-averaged cross-section of $4.4 \times 10^{-26} \text{ cm}^3 \text{ ss}^{-1}$. Adapted from Ref. [30]. (For interpretation of the references to colour in this figure legend, the reader is referred to the web version of this article.)

2.8. Observations of the galactic halo and centre

The Galactic Centre (GC) is a long-discussed target for indirect DM searches with Cherenkov telescopes [114]. The density of the DM halo should be highest in the very centre of the Milky Way, giving rise to a gamma-ray flux from annihilation of DM particles. On the one hand, this view is strengthened by the results of recent *N*-body simulations of CDM halos [115] suggesting that, for an observer within the Milky Way, the annihilation signal from DM is not primarily due to small subhalos, but is dominated by the radiation produced by diffuse DM in the main halo. On the other hand, searches close to the GC are made difficult by the presence of the Galactic Centre source HESS J1745–290 [116,117] and of diffuse emission from the Galactic plane [118]. Both emissions can be plausibly explained by astrophysical emission processes: HESS J1745–290 is thought to be related to the Black Hole Sgr A* or the pulsar wind nebula G 359.95–0.04 [119], and the diffuse emission is well described as arising from hadronic cosmic rays interacting in giant molecular clouds. In both cases, the measured energy spectra do not fit DM model spectra [120] and thus make a dominant contribution from DM annihilation or decay unlikely.

In this situation, DM searches should better target regions which are outside the Galactic plane and hence not polluted by astrophysical gamma-ray emission, but which are still close enough to the GC to exhibit a sizable gamma-ray flux from DM annihilation in the Milky Way halo [121]. Given the angular resolution of Cherenkov telescopes and the scale height of the diffuse emission from the Galactic plane these criteria are fulfilled for an angular distance of about $0.3°$ from the GC. This angular scale translates into a distance of 45 pc from GC when using 8.5 kpc as the galactocentric distance. The radial DM density profiles obtained in *N*-body simulations of Milky Way sized galaxies, like Aquarius [115] and via Lactea II [122], can be described by Einasto and NFW parameterizations, respectively. These parameterizations differ substantially when extrapolating to the very centre of the Milky Way halo since the NFW profile is much more strongly peaked. At distances greater than about 10 pc, the difference is, however, just a factor of 2 which implies that a search at angular scales of $> 0.3°$ will not be hampered by the imprecise knowledge of the DM density profile at small scales.

A search for a DM annihilation signal from the halo at angular distances between $0.3°$ and $1.0°$ from the GC has recently been performed using 112 h of H.E.S.S. data [42]. For WIMP masses well above the H.E.S.S. energy threshold of 100 GeV this analysis provides the currently most constraining limits on the velocity averaged annihilation cross section $(\sigma_{ann} v)$ of WIMPs (for IACTs) at the level of few 10^{-25} cm^3 s^{-1}. Towards lower WIMP masses, observations of dwarf galaxies with the Fermi-LAT satellite yield even better limits [49] demonstrating how both observations of dwarf galaxies and of the extended GC region allow to jointly constrain the parameter space.

2.9. Simulations and assumptions

The prospects of a search for DM annihilation photons from the Milky Way halo with CTA depend on (i) the performance of the southern CTA array, (ii) the applied analysis and background rejection techniques, and (iii) the details of the DM distribution and WIMP annihilation. At low energies, the sensitivity of IACTs is limited by the presence of hadron and electron showers which arrive isotropically and which can only be distinguished from photons on a statistical basis. The basic strategy for the halo analysis is therefore to compare the fluxes of gamma-like events from a signal region (with solid angle $\Delta\Omega_s$) and a background region (solid angle $\Delta\Omega_b$) and to search for DM features in the background-subtracted energy spectra. The signal region can be chosen such that it has

the same instrumental acceptance as the background region, but is located closer to the GC and features therefore a higher DM annihilation flux. For the purpose of this section, we rewrite Eq. (1.1) in terms of differential DM photon *rate* expected from the signal or background regions (s, b respectively), given by:

$$\frac{dR}{dE}\bigg|_{s,b} = \frac{(\sigma_{ann} v)}{8\pi m_\chi^2} \frac{dN_\gamma}{dE_\gamma} \int_{\Delta\Omega_{s,b}} J(\Omega)A(\Omega,E)d\Omega, \qquad (1.3)$$

where dN_γ/dE_γ is the photon spectrum generated in the annihilation of a WIMP of mass m_χ, and $A(\Omega,E)$ are the CTA effective areas for photons, which depend on the position of the region within the FOV (Ω), the energy E and further parameters (like the zenith angle of the observations). $J(\Omega)$ is the line-of-sight integral over the squared DM density $\rho(r)$ (cf. Eq. (1.2)). Since the DM density depends only on the distance to the GC r the line-of-sight integral and the astrophysical factor are only a function of the angular distance ψ from the GC. Assuming that the signal and background region differ only with respect to their DM annihilation flux and their relative size $\alpha = \Delta\Omega_s/\Delta\Omega_b$, the rate of excess photon events $R_s - \alpha R_b$ is given by

$$\frac{(\sigma_{ann} v)}{8\pi m_\chi^2} \int_0^\infty dE \frac{dN_\gamma}{dE_\gamma} \left[\int_{\Delta\Omega_s} J(\psi)A(\Omega,E)d\Omega - \alpha \int_{\Delta\Omega_b} J(\psi)A(\Omega,E)d\Omega \right]. \qquad (1.4)$$

Clearly, the rate vanishes when the astrophysical factors of the signal and the background regions are identical which implies that in the case of an isothermal DM density profile, a halo analysis with signal and background region chosen too close to the GC will not allow the placement of limits on $(\sigma_{ann} v)$.

Given an observation time T, Eq. (1.4) can be used to estimate the number of excess photons for a particular realization of CTA and a DM model defining $(\sigma_{ann} v), dN_\gamma/dE_\gamma$ and $J(\psi)$. Equivalently, one can place a limit on $(\sigma_{ann} v)$ given an upper limit on the number of excess photon events. Simulations of the candidate arrays E and B at a zenith angle of $20°$ were used to infer the effective area for diffuse photons and the residual rate of protons anywhere in the FOV. Both arrays feature large-size telescopes and are therefore suitable for studies in the low-energy domain. The available observation time was set to 100 h, which is about 10% of the total observation time per year. Two different ways of defining signal and background regions were employed and compared, namely the so-called *Ring Method* and the On–Off Method. For the *Ring Method*, the candidate arrays E or B were assumed to observe the GC region at Galactic longitude $l = 0$ and Galactic altitude b, and signal and background regions were placed in the same FOV as illustrated in Fig. 8. An annulus with inner radius r_1 and outer radius r_2 around the observation position was constructed and divided into signal and background region such that the signal region is closer to the GC and has therefore a larger astrophysical factor. The separation of signal and background region is achieved by a circle with radius Δ_{cut} around the GC whose intersection with the annulus defines the signal region. All other regions on the ring were considered as background region. The values of the four parameters b, r_1, r_2 and Δ_{cut} were optimized such that the attained significance of a DM signal per square root time was maximized. The maximization was carried out for a wide range of WIMP masses but the dependence on the actual WIMP mass was found to be fairly weak. The derived values for both candidate arrays are listed in Table 1.2. Judging from present IACT observations, we do not expect strong diffuse gamma-ray emission to extend outside the $\pm0.3°$ box used to mask the galactic disc. New point-like or slightly extended sources will be excluded, making the On and Off region smaller. In addition, the approach is only sensitive to gradients in the diffuse gamma-ray emission, whereas the charged particle
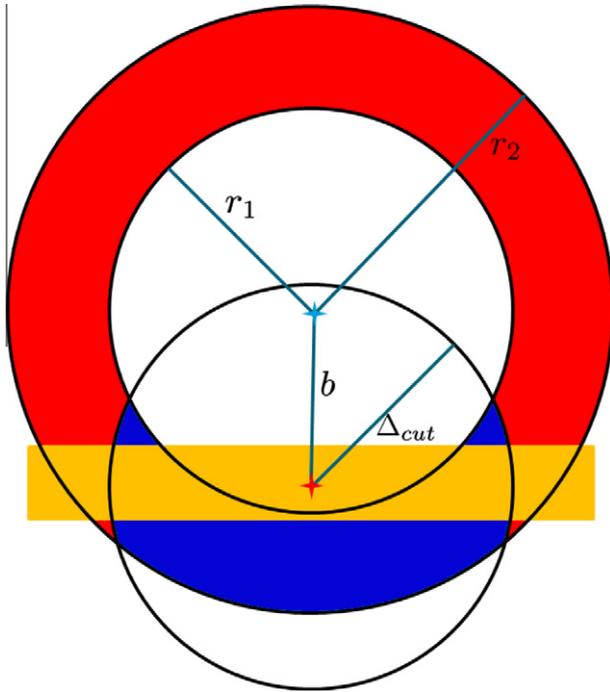
Fig. 8. Illustration of the *Ring Method* for constructing signal and background regions within one FOV of the CTA candidate arrays. The red star denotes the position of the GC in galactic coordinates; the blue star marks the pointing position of the CTA array which is shifted by an amount b in latitude from the GC. The annulus with inner and outer radii r_1 and r_2 around the observation position defines regions of equal acceptance. The signal region (blue, close to the GC) is constructed as intersection of the annulus and a circle around the GC with radius Δ_{cut}. The remaining regions on the annulus (red) are used as background region. Regions within $\pm 0.3°$ of the galactic plane (yellow) are neither part of the signal nor of the background region. (For interpretation of the references to colour in this figure legend, the reader is referred to the web version of this article.)

background is isotropic. In the optimization process an Einasto profile was assumed for the DM signal, but the optimal values are only weakly dependent on the assumed profile in the region beyond 0.3 degrees from the Galactic plane.

The usage of the annulus implies the same acceptance for signal and background region since the acceptance is, to good approximation, only a function of the distance to the observation position. Placing both signal and background regions in the same FOV implies that both regions will be affected by time-dependent effects in a similar way. A disadvantage is, however, that the angular distance between the signal and background region is only of order of the FOV diameter, reducing the contrast in Eq. (1.4) considerably. This contrast was increased in the On–Off Method where data-taking with an offset of typically 30' in Right Ascension was assumed. In this mode, the telescopes first track for half an hour the same observation position as in the *Ring Method* which defines the signal region. The telescopes then slew back and follow the same path on the sky for another 30 min. The second pointing has the same acceptance as the first one since the same azimuth and zenith angles are covered but generates a background region with much increased angular distance to the GC. In the On–Off Method, the observation time was 50 h for the signal and 50 h for the back-

Table 1.2
Optimized values of the parameters used in the application of the *Ring Method* for the candidate arrays E and B. See Fig. 8 for a description of the parameters.

Array	b	r_1	r_2	Δ_{cut}
E	1.42°	0.55°	2.88°	1.36°
B	1.40°	0.44°	2.50°	1.29°

Table 1.3
Astrophysical factor for the signal region and size of the integration region ($\Delta\Omega$) for *Ring* and on–off method. In the case of the on–off method, $\Delta\Omega$ was chosen as the entire FOV of the candidate array which introduces a dependence on the assumed WIMP mass since the effective FOV grows with photon energy. The table gives values for a WIMP mass of 0.1, 1, and 10 TeV.

Method	Array (TeV)	m_χ	$\tilde{J}_s$ (10^{22} GeV^2 cm^{-5})	$\Delta\Omega$ (sr)
Ring	E	Any	4.68	0.00117
	B	Any	4.43	0.00104
On–off	E	0.1	16.4	0.00751
		1	19.7	0.01044
		10	28.7	0.02211
On–off	B	0.1	16.4	0.00751
		1	22.8	0.01384
		10	28.7	0.02211

ground region giving again a total observation time of 100 h. Regardless of whether the *Ring Method* or the On–Off Method was used, all areas with $|b| < 0.3°$ were excluded from signal and background regions to avoid pollution from astrophysical gamma-rays.

The astrophysical factor (Eq. (1.2)) was taken from the Aquarius Simulation [115] which had been corrected for the presence of subhalos below the resolution limit of the simulation. The line-of-sight integral assumes a value of 40.3×10^{24} GeV^2 cm^{-5} sr^{-1} at $\Psi = 1°$. Table 1.3 lists the astrophysical factors of the signal regions which were defined in the Ring and On–Off Method, respectively. In case of the On–Off Method, the signal region was defined as the total effective FOV of the On–pointing which introduces a dependence on the WIMP mass since the FOV grows with photon energy. For the WIMP annihilation spectrum dN_γ/dE_γ several different choices were considered. The generic Tasitsiomi spectrum [60] is appropriate for a dominant annihilation into quark-antiquark pairs with subsequent hadronization into π^0 particles and was used in the optimization of the parameters of the *Ring Method*. Other spectra were explored by considering $b\bar{b}, \tau^+\tau^-$ and $\mu^+\mu^-$ final states [88].

2.10. Discussion

The two plots in Fig. 9 show the upper limits for WIMP masses between 0.1 TeV and 10 TeV, translated from the sensitivity using here the method of [59]. Each curve corresponds to one set of assumptions. It is evident that the most constraining limits can be derived for masses of about 0.5 TeV which is a factor of 2 improvement compared to current IACT arrays like H.E.S.S. reaching best sensitivity around 1 TeV. This is a direct consequence of the lower threshold and superior stereoscopic background rejection of the CTA candidate arrays. Typical limits are around few 10^{-26} cm^3 s^{-1} which is a factor of 10 improvement compared to current IACTs. The comparison of array E (blue) and B (same line style but red) shows that the limits for array B are always better, which can be understood from the fact that B comprises 5 large-size telescopes and array E only 4. The magnitude of this effect is, however, comparatively small ($\sim 20\%$). Overall, CTA should be able to probe the parameter space below the velocity averaged annihilation cross-section for thermally produced DM of 3×10^{-26} cm^3 s^{-1} for WIMP masses between several ten GeV and several TeV.

The upper panel of Fig. 9 illustrates the impact of data-taking with the *Ring Method* and the On–Off Method for the case of a dominant annihilation into quark-antiquark pairs with subsequent π^0 creation [60]. The On–Off Method (dashed lines) is more sensitive than the *Ring Method* (dashed lines). One must keep in mind, however, that the On–Off Method spends 50% of the observation time far away from the GC which implies that this data set will
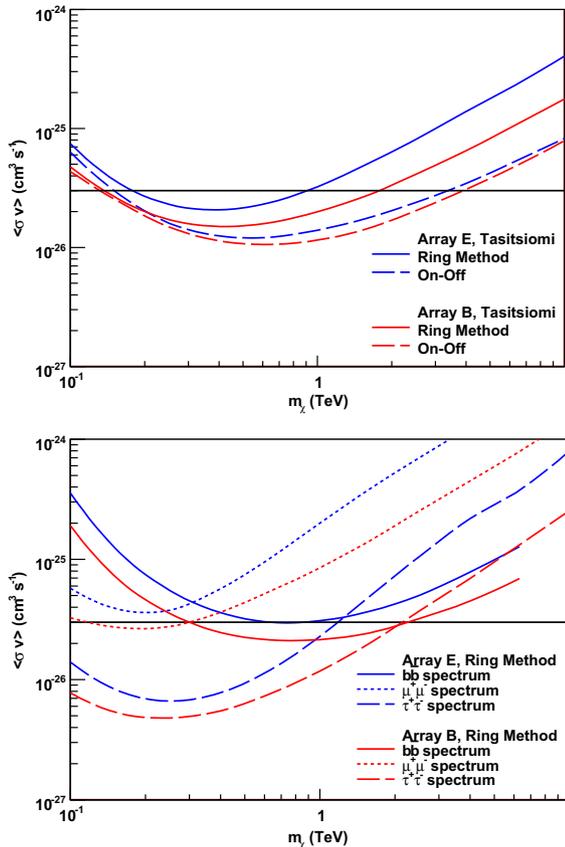
Fig. 9. CTA sensitivities on the velocity averaged annihilation cross-section as a function of the WIMP mass. Shown are curves for the candidate arrays *E* (blue) and *B* (red). **Top:** Comparison of the *Ring Method* (solid lines) and On–Off Method for background subtraction. Annihilation as in [60] was assumed. **Bottom:** Comparison of different WIMP spectra for the *Ring Method*. The solid line denotes the case of annihilation into $b\bar{b}$; $\mu^+\mu^-$ and $\tau^+\tau^-$ spectra are shown by the dotted and dashed lines, respectively. On both panels, the classical annihilation cross section for thermally produced WIMPs at 3×10^{-26} cm³ s⁻¹ is indicated by the black horizontal line. (For interpretation of the references to colour in this figure legend, the reader is referred to the web version of this article.)

be of limited use for studies of astrophysical sources. Another drawback of the On–Off Method is its susceptibility to systematic effects arising from variations of the data-taking conditions (electronics, atmosphere). In view of this, the increased sensitivity for the DM halo analysis in parts of the parameter space will not probably suffice to motivate the acquisition of a larger data set in this mode.

Compared with the choice of the CTA candidate array (*B* or *E*) and the analysis method (*Ring Method* or On–Off Methods), the WIMP annihilation spectrum has the strongest impact on the CTA sensitivity. The lower panel of Fig. 9 shows for both candidate arrays and the *Ring Method* the limits obtained in the case of a dominant annihilation into $b\bar{b}$ pairs (solid), $\mu^+\mu^-$ (dotted) and $\tau^+\tau^-$ (dashed). The small photon yield from $\mu^+\mu^-$ final states implies limits that are a factor of about 5 worse than limits for dominant annihilation into $\tau^+\tau^-$. It is clear that the full potential of the halo analysis will be exploited by confronting individual DM models with their predicted WIMP annihilation spectra dN_γ/dE_γ with data.

2.11. Anisotropies in the diffuse gamma-ray background

Besides gamma-rays from individual resolved sources and Galactic foreground, another component of diffuse gamma-ray background radiation has been detected and proven to be nearly isotropic. This radiation dominantly originates from conventional unresolved point sources below the detection threshold, while another fraction might be generated by self-annihilating (or decaying) DM particles, which then could produce specific signatures in the anisotropy power spectrum of the diffuse gamma-ray background [123–127]. The different hypotheses about the origin of the gamma-ray background may be distinguishable by accurately measuring its anisotropy power spectrum.

Compared to the current generation of IACTs, CTA will have improved capabilities to measure anisotropies in the diffuse gamma-ray background, based upon a better angular resolution (determined by the point-spread function, PSF), an increased size of the FOV, and a higher background rejection efficiency. In the following, we discuss the effects of different assumptions on the background level and the anisotropy spectrum on the reconstruction of the power spectrum for the current generation of IACTs, and address the improvement obtainable with CTA. Finally, we make predictions for the discrimination between astrophysical and dark matter induced anisotropy power spectra for CTA.

2.12. Simulation

In order to investigate the measured power spectrum and the impact of instrumental characteristics, a sample of *event lists* containing anisotropies generated with Monte-Carlo simulations was analyzed. The event lists were simulated by generating skymaps with a given anisotropy power spectrum. In total, 12 skymaps covering the size of the FOV and being in different celestial positions were created, with a power spectrum for a given multipole moment ℓ defined as $C_\ell = 1/(2\ell+1) \sum |a_{\ell m}|^2$, $m = -\ell, \dots, \ell$, where $a_{\ell m}$ denotes the coefficients of a (real-valued) spherical function decomposed into spherical harmonics. With $\langle a_{\ell m} \rangle = 0$, C_ℓ reflects the width of the $a_{\ell m}$ distribution, which was assumed to be Gaussian. The simulations were made for different power spectra $\ell(\ell+1)C_\ell \sim \ell^s$, with $s = 0.5, 1.0, 1.5, 2.0, 2.5$. The pixel size of these skymaps was 0.002°, corresponding to $\ell = 9 \times 10^4$ (where $\Theta_\ell = 180°/\ell$). The skymaps $I(\vartheta, \varphi)$ were normalized in a way that the pixel with the smallest signal was assigned the value 0 and the pixel with the largest signal was assigned 1. Anisotropy power spectra were then derived from the fluctuation maps $I(\vartheta, \varphi)/\langle I \rangle$, such that for a *full signal* the maximum allowed difference in each map equals 1. Note that this difference can be smaller when an additional isotropic *noise* component is present.

An event was simulated in three subsequent steps: First, the celestial position was randomly chosen within the FOV, and the event was classified to represent a *signal*- or isotropic *noise*-event, respectively. The decision for a signal event was based upon a normalized random number z: If z was smaller than the skymap value at the corresponding position, the event was considered a signal event. Otherwise, another event position was selected while reapplying the procedure. Subsequently, the event map was convolved with a PSF of 0.1°, which is similar to the resolution of current IACTs. The effect of a better angular resolution is discussed below. The event maps were simulated to contain 10^7 entries. Note here that this number, as selected for the toy model, does in general not reflect the actual number of expected physical signal events. Therefore, the following discussion is focussed more on a qualitative discussion of the criticalities of the calculation rather than on making quantitative predictions.

To analyze an event list containing N_{ev} events, a HEALPix skymap with N_{pix} pixels was accordingly filled, and analyzed using the HEALPix software package.[3] Therefore, the analyzed function is

$$w(\hat{n})f(\hat{n}) = \frac{N_{pix}}{N_{event}} \sum_{i=1}^{N_{pix}} x_i \cdot b_i(\hat{n}),$$ (1.5)

---

[3] http://healpix.jpl.nasa.gov/.

where x_i denotes the number of events in pixel i, and $b_i(\hat{n})$ equals 1 inside pixel i and 0 outside. The function $w(\hat{n})$ describes the windowing function – in this case the FOV with Gaussian acceptance – and $f(\hat{n})$ denotes the original signal function over the full sky. The windowing function was normalized such that the integral over the full sky equals 4π:

$$\int d\Omega\, w(\hat{n}) f(\hat{n}) = 4\pi. \qquad (1.6)$$

Note that this differs from other analyses of this type, where w is defined such that the maximum value is 1. This difference in the normalization was done in order to keep a simple simulation code, and results should be equivalent. Final results were averaged over the corresponding 12 skymaps.

2.12.1. The effect of the anisotropy spectrum and the residual background level on the spectral reconstruction

In Fig. 10, we show the mean value and the RMS of the C_ℓ power spectra. The value C_ℓ represents the strength of anisotropies of the angular scale $\Theta_\ell = 180°/\ell$. Anisotropies smaller than the angular resolution (defined by the PSF) are smeared out. This effect is clearly visible for large $\ell \geqslant 1000$, where the power spectra converge into the Poissonian noise of the isotropic background spectrum. The angular resolution assumed for the simulation shown in this figure has a width of $\sigma_{PSF} = 0.1°$. Furthermore, anisotropies with a size larger than the FOV are truncated at $\ell \sim 100$ due to the effect of the windowing function. The simulated FOV in Fig. 10 has a width of $2.5°$, which is comparable with the FOV of current IACT experiments. For the toy model, Fig. 10 demonstrates that, for $\ell \sim 100 - 1000$, power spectra of different slopes are separable within the statistical errors and distinguishable from isotropic noise. CTA will have a smaller PSF as well as a larger FOV. This will make the signal vanish at larger ℓ than in the example, and the windowing function will influence the spectrum to smaller ℓ than in the figure. Therefore, we conclude that the FOV as well as the PSF, while important, will not be crucial for the investigation of anisotropies with CTA in the desired multipole range.

In general, the measured flux will be composed of both signal and background events. The background is produced mainly by two separate processes:

1. Events caused by cosmic rays (protons and electrons) which are misinterpreted as photon events.
2. An isotropic component of the photon background radiation, which does not count as *signal* according to our definition.

The influence of isotropic background is demonstrated in Fig. 11, where the power spectrum for $s = 0.5$ is shown for different background levels. Here, the signal fraction is defined by $f_{sig} = N_{sig}/N_{ev}$, where N_{sig} denotes the number of signal events. The overall power is clearly reduced in case of fully isotropic background. From the figure, we see that when the signal fraction improves by a factor 5, the power spectrum is boosted by about two orders of magnitude. For this reason, we expect the ten-fold improved CTA sensitivity to mark the major difference with respect to the current generation of IACTs for such studies.

2.12.2. Prospects for astrophysical and dark matter anisotropies discrimination

The theoretical expectations for the power spectra of the diffuse gamma-ray flux of both the astrophysical as well as the DM components are highly model dependent. Since the astrophysical component is dominated by the gamma-ray flux from unresolved point sources, expected with a constant C_ℓ ($s = 2.0$ in our notation), we conservatively assume the slope of the DM component (s) to be
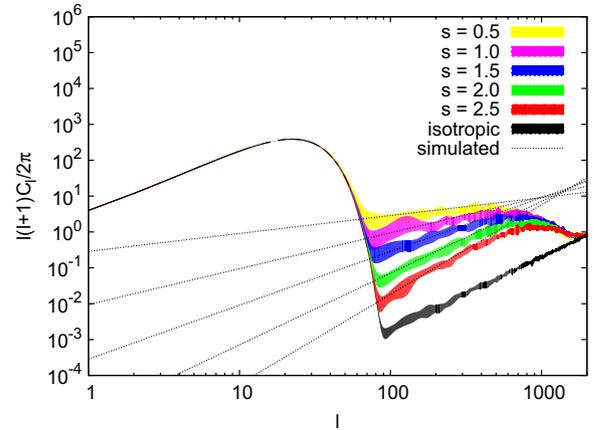

Fig. 10. Measured power spectra $l(l+1)C_\ell/(2\pi)$ for different slopes s of the simulated input spectrum, compared to an isotropic background spectrum. Color-filled areas depict the RMS of the spectra. The size of the PSF is $\sigma_{PSF} = 0.1°$. For reference, the simulated spectra are shown as dashed lines. (For interpretation of the references to colour in this figure legend, the reader is referred to the web version of this article.)
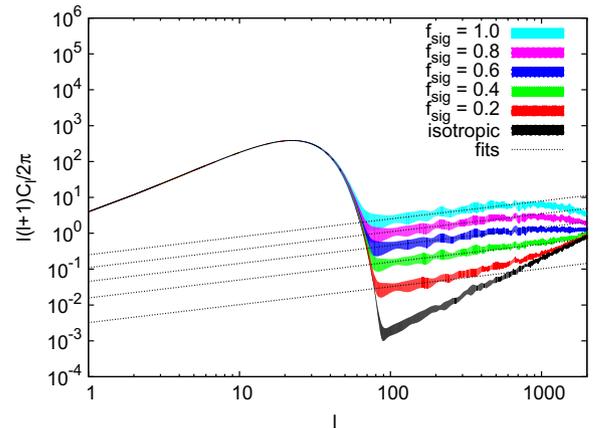

Fig. 11. Influence of the signal fraction on the measured power spectrum. Shown are the reproduced spectra for a slope $s = 0.5$ for several ratios between signal and total events; the *background* events are distributed isotropically. In order to estimate the effect of the noise ratio, the best fit levels are shown as dotted lines. The width of the PSF is chosen as in Fig. 12, $\sigma_{PSF} = 0.05°$.

similar. In this scenario, the difference between the power spectra manifests in the normalization. For unresolved point sources, $C_{\ell,blazars} = 10^{-5}$, while for DM-induced anisotropies, considering the thermal annihilation cross-section 3×10^{-26} cm^3 s^{-1}, $C_{\ell,DM} = 10^{-3}$ is expected (see, e.g., [127]). In our simulation, this was realized by distributing $N = 4\pi/C_\ell$ point sources over the full sky. While representing a non-physical model, this is a convenient way of producing a Poissonian anisotropy power spectrum which is a reasonable assumption for generic astrophysical and DM emitters. The normalization of the signal was set by extrapolating the spectrum of the extragalactic gamma-ray background (EGB) [128] to $E > 100$ GeV. Note that the strength of the DM annihilation signal is strongly affected by the formation histories of DM halos and the distribution of DM subhalos. For example, Fig. 3 in [129] shows that the gamma-ray spectrum of DM annihilation could reach the measured gamma-ray background spectrum and therefore deliver a significant fraction of the measured flux. Here, we investigate the cases that (a) the total EGB originates from astrophysical sources and (b) 20% of the EGB (optimistically) originates from DM annihilation. The isotropic hadronic component depends on analysis cuts and the
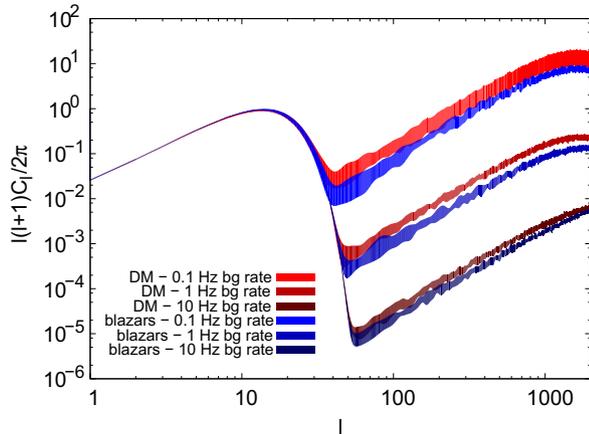
Fig. 12. Comparison between measured anisotropy power spectra with (a) a pure astrophysical origin represented by $C_\ell = 10^{-5}$ (blue bands) and (b) with an additional DM component, i.e., 20% of the total flux, represented by $C_\ell = 10^{-3}$ (red bands). The assumed observation time is 300 h. The three cases in each plot represent the hadronic background rates of 10 Hz, 1 Hz, and 0.1 Hz.

quality of the gamma-hadron separation. In the following, three different background rates are assumed: 10 Hz, 1 Hz, and an optimistic 0.1 Hz rate. We assume a CTA-like FOV with a radius of 5° and a CTA-like PSF with $\sigma_{PSF} = 0.05°$. The results are shown in Fig. 12, where each band represents a sample of 20 realizations. One can see in the figure that depending on the achieved background rate, in principle the two above mentioned scenarios (a) and (b) will be well distinguishable for CTA.

3. Search of axion-like particles with CTA

Axions were proposed in the 1970's as a by-product of the Peccei-Quinn solution of the strong-CP problem in QCD [130]. In addition, they are valid candidates to constitute a portion of, or perhaps the totality of, the non-baryonic CDM content predicted to exist in the Universe. Another extremely interesting property of axions, or more generically, Axion-Like Particles (ALPs, for which – unlike axions – the mass m_a and the coupling constant are not related to each other), is that they are expected to convert into photons (and *vice versa*) in the presence of magnetic fields [131,132]. The photon/ALP mixing is indeed the main signature used at present in ALP searches, such as those carried out by CAST [133–136] or ADMX [137], but it could also have important implications for astronomical observations. For example, photon/ALP mixing could distort the spectra of gamma-ray sources, such as Active Galactic Nuclei (AGN) [138–141] or galactic sources, in the TeV range [142].

The photon/ALP mixing effect for distant AGN was also evaluated by [143] under a consistent framework, where mixing takes place inside or near the gamma-ray emitter as well as in the intergalactic magnetic field (IGMF). A diagram that outlines this scenario is shown in Fig. 13. The artistic sketch shows the travel of a photon from the source to the Earth and the main physical cases that one could identify.[4] From top to bottom: (1) the photon converts to an axion and back to photon in the IGMF, (2) the photon converts to an axion in the IGMF, (3) the photon converts to an axion at the source, which then does not interact with the EBL, therefore traveling unimpeded from the source to the Earth, (4) the photon travels unimpeded from the source to the Earth, (5) the photon converts to an axion at the source and back to photon in the IGMF, (6) the pho-

ton interacts an EBL photon resulting in pair production. It is clear that cases 2, 3, 6 corresponds to an attenuation of the intrinsic source flux, while cases 1, 4, 5 allow for a recovery of the intrinsic photon yield.

The probability of a photon of energy E_γ to be converted into an ALP (and *vice versa*) can be written as [138]:

$$P_0 = \frac{1}{1 + (E_{crit}/E_\gamma)^2} \sin^2\left[\frac{Bs}{2M}\sqrt{1 + \left(\frac{E_{crit}}{E_\gamma}\right)^2}\right] \tag{2.1}$$

where s is the length of the domain where there is a roughly constant magnetic field B, and M the inverse of the coupling constant. Here we also defined a characteristic energy, E_{crit}:

$$E_{crit} \equiv \frac{m^2 M}{2B} \tag{2.2}$$

or in more convenient units:

$$E_{crit}(GeV) \equiv \frac{m_{\mu eV}^2 M_{11}}{0.4 B_G} \tag{2.3}$$

where the subindices refer to dimensionless quantities: $m_{\mu eV} \equiv m/\mu eV$, $M_{11} \equiv M/10^{11}$ GeV and $B_G \equiv B/Gauss$; m is the effective ALP mass $m^2 \equiv |m_a^2 - \omega_{pl}^2|$, with $\omega_{pl} = 0.37 \times 10^{-4}\, \mu eV \sqrt{n_e/cm^{-3}}$ the plasma frequency and n_e the electron density. The most recent results from the CAST experiment [136] give a value of $M_{11} \geqslant 0.114$ for ALP mass $m_a \leqslant 0.02$ eV. At present, the CAST bound is the most general and stringent limit in the range 10^{-11} eV $\ll m_a \ll 10^{-2}$ eV.

The main effect produced by photon/ALP mixing in the source is an *attenuation* in the total expected intensity of the source just above a critical energy E_{crit} (see Fig. 13). As for the mixing in the IGMFs, despite the low magnetic field B, the photon/ALP conversion can take place due to the large distances involved. In the model of [143], it is assumed that the photon beam propagates over N domains of a given length. The modulus of the IGMF is the same in all of them, whereas its orientation changes randomly from one domain to the next, which in practice is also equivalent to a variation in the strength of the component of the magnetic field relevant to the photon/ALP mixing.

In discussing photon/ALP conversion in IGMFs, it is also necessary to consider the important role of the Extragalactic Background Light (EBL), its main effect being an additional attenuation of the photon flux (especially at energies above about 100 GeV). Recent gamma-ray observations already pose substantial challenges to the conventional models that explain the observed source spectra in terms of EBL attenuation [144–148].

Taken together, photon/ALP conversions in the IGMF can lead to an *attenuation* or an *enhancement* of the photon flux at Earth, depending on distance, magnetic fields and the EBL model considered. A flux enhancement is possible because ALPs travel unimpeded through the EBL, and a fraction of them can convert back into photons before reaching the observer. Note that the strength of the IGMFs is expected to be many orders of magnitude weaker ($\sim$nG) than that of the source and its surroundings ($\sim$G). Consequently, as described by Eq. (2.3), the energy at which photon/ALP conversion occurs in this case is many orders of magnitude larger than that at which conversion can occur in the source and its vicinity. Assuming a mid-value of B$\sim$0.1 nG, and $M_{11} = 0.114$ (CAST lower limit), the effect could be observationally detectable by IACTs only if the ALP mass is of the order of 10^{-10} eV, i.e., we need ultra-light ALPs.

In order to quantitatively study the effect of photon-axion conversion over the cosmological distances of AGN, we consider the total photon intensity. It becomes then useful to define the *axion boost factor* as the difference between the predicted arriving photon intensity without including ALPs and that obtained when

---

[4] Note that this formalism neglects, however, the mixing that may happen inside the Milky Way due to galactic magnetic fields. In the most idealistic/optimistic case, it would produce a photon flux enhancement at Earth of $\sim$3% [141].
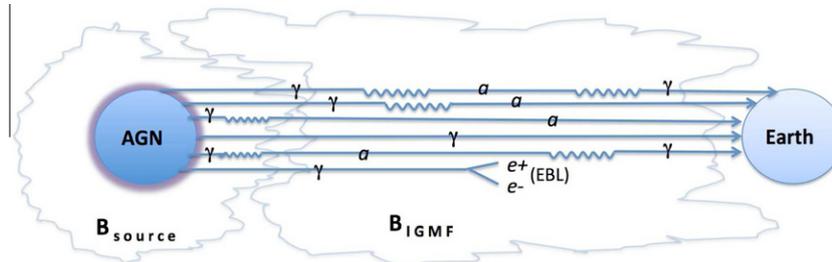
**Fig. 13.** Photon/ALP conversions (crooked lines) that can occur in the emission from a cosmological source. γ and a symbols represent gamma-ray photons and ALPs respectively. This diagram collects the main physical scenarios that we might identify inside our formalism. Each of them are schematically represented by a line that goes from the source to the Earth. From [143].

including the photon/ALP conversions. Qualitatively speaking, it is found that the more attenuating the EBL model considered, the more relevant the effect of photon/ALP conversions in the IGMF (since any ALP to photon reconversion might substantially enhance the intensity arriving at Earth). Furthermore, higher B values do not necessarily translate into higher photon flux enhancements. There is always a B value that maximizes the axion boost factors; this value is sensitive to the source distance, the considered energy and the adopted EBL model (see Ref. [143] for a more detailed discussion).

There could be indeed different approaches from the observational point of view, although all of them will be probably based on the search and analysis of a systematic residual after applying the best-fit (conventional) model to the AGN data. For example, Ref. [143] predicts the existence of a universal feature in the spectrum of the sources due to the intergalactic mixing, that is completely independent on the sources themselves and only depends on the ALP and IGMF properties. This feature should be present at the same critical energy E_{crit} for all sources, and would show up in the spectra as a drop in the flux – whenever E_{crit} is in the range where the EBL effect is negligible – or even as a sudden flux increase, if the EBL absorption is strong for $E = E_{crit}$.

3.1. Test case for CTA: PKS 1222 + 21

We have taken as a test source the flat spectrum radio quasar 4C + 21.35 (PKS 1222 + 21), at redshift $z = 0.432$, which was detected by MAGIC above 70 GeV [149] in June 2010, during a *target of opportunity* observation triggered by the high state of the source in the Fermi-LAT energy band. This source is the second most distant object detected by ground-based gamma-ray telescopes, and hence an ideal candidate for the study of propagation effects. The observed energy spectrum of 4C + 21.35 during the 0.5 h flare recorded by MAGIC was well described by a power law of index $\Gamma = 3.75 \pm 0.27_{stat} \pm 0.2_{syst}$. The intrinsic spectrum, assuming the EBL model of [150] was estimated to be a power law of index $\Gamma = 2.72 \pm 0.34$, which extrapolated down to an energy of about 5 GeV, connects smoothly with the harder spectrum ($\Gamma = 1.95 \pm 0.21$) measured by Fermi-LAT between 0.2 and 2 GeV in a 2.5 h period encompassing the MAGIC observation. It must be noted that longer-term Fermi-LAT observations of the source in various states of activity show a break in the spectrum between 1 and 3 GeV, with a spectral index after the break (and up to $\simeq 50$ GeV) ranging between 2.4 and 2.8 [151].

We have simulated CTA observations of 4C + 21.35 assuming an intrinsic unbroken power-law spectrum, in the relevant energy range, like the one determined by MAGIC for 4C + 21.35 during the flare, i.e., $dN/dE = K \times [E/(0.2 \text{ TeV})]^{-2.72}$. Keeping the spectral shape unchanged, we have tried different absolute flux normalizations, taking as a reference the flux observed by MAGIC, $K = 1.78 \times 10^{-5}$ m^{-2} s s^{-1} TeVs^{-1}. We have also tested different

observation times: the actual duration of the VHE flare observed by MAGIC is unknown, since the observation was interrupted while the flare was still going on, but the flares observed by Fermi-LAT above 100 MeV show rise and decay time scales of the order of a day [151], so it is reasonable to expect that the source may stay several hours in flux states as high as that observed by MAGIC. For the detector simulation we have used the CTA candidate array E. The EBL model in Ref. [150] has been used to account for the effect of the EBL, and the conversion of photons into ALPs and *vice versa* has been simulated following the formalism detailed in Ref. [143] as outlined above. Only conversions in the IGMF have been considered (in this case, mixing in the source typically leads to only a few percent of flux attenuation, so we neglected it in order to avoid extra uncertainties).

We have assumed the same parameters for the IGMF as those in the fiducial model in [143]: 0.1 nG is the (constant) modulus of the IGMF,[5] which is assumed to have fixed orientation within domains of size 1 Mpc. The orientation of the IGMF varies randomly from one domain to the next. The ALP parameters, mass and coupling constant, enter via E_{crit}, below which the conversion probability is negligible. We have scanned E_{crit} in the range 0.1 to 10 TeV in steps of 0.1 TeV.

Using the performance parameters of array E, we obtain the expected gamma-ray and cosmic-ray background rates in bins of estimated energy, and from them the reconstructed differential energy spectrum. After this, we correct the observed spectrum by the energy-dependent attenuation factors expected from the EBL in order to get an estimate of the intrinsic source spectrum. Each simulated spectrum is fitted to a power-law with variable index of the form $dN/dE \propto E^{-\alpha - \beta \log(E/0.1 \text{ TeV})}$, in which we constrain the β parameter so that the spectrum cannot become harder with increasing energy (such behavior is not expected from emission models in this energy range). Only energy bins with a signal exceeding three times the RMS of the background, and a minimum of 10 excess events, are considered in the fit.

In the absence of any significant photon/ALP mixing, the resulting fits will all match the spectral points within the experimental uncertainties, resulting in *good* χ^2 values. But, as shown in Ref. [143], certain combinations of ALP parameters and values of the IGMF may result in significant modifications of the observed VHE spectra. The most striking feature is a *boost* of the expected flux at high energies, which is particularly prominent in the estimated intrinsic (i.e., EBL-de-absorbed) spectrum. Such a feature may result in a low value of the χ^2-probability of the spectral fit. In Figs. 14 and 15 we show two such cases, in which the observed spectra, after de-absorption of the EBL effect, show a clear hardening of the

---

[5] Note that this is just one order of magnitude below the current upper limits [152], and lower limits lie many orders of magnitude below [153,154]. With a IGMF of 0.01 nG or smaller the effect of the photon/ALP mixing would probably be too weak to be observed with CTA.
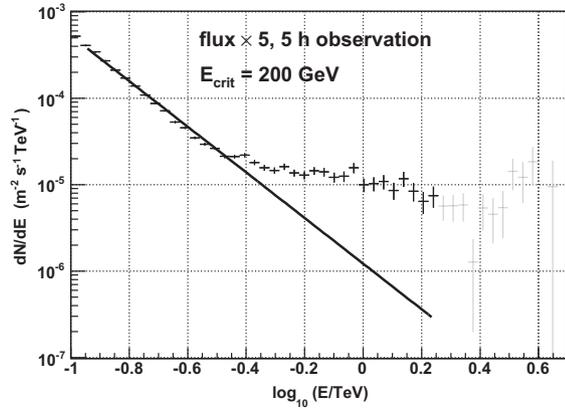
Fig. 14. Simulation of a 5 h CTA observation of a 4C + 21.35 flare 5 times more intense than the one recorded by MAGIC [149]. In black, energy bins used for the fit (those with a signal exceeding three times the RMS of the background, and a minimum of 10 excess events). Excluded points are displayed in grey. The estimated intrinsic differential energy spectrum (after correcting for the EBL effect) shows a *boost* at high energies due to photon/ALP mixing. The IGMF strength is assumed to be 0.1 nG, and ALP parameters result in $E_{crit} = 200$ GeV.

Fig. 16. Median of the χ^2-probabilities of the fits to the de-absorbed differential energy spectra of 4C + 21.35 measured by CTA, assuming photon/ALP mixing, for different values of E_{crit}. We simulated observations of flares of two different durations: 0.5 and 5 h, and with intensities equal to 1 and 5 times that of the flare reported in [149]. The dashed horizontal line marks the probability that corresponds to 5 standard deviations.

spectral index. The effect is particularly striking in the cases in which the EBL absorption at $E = E_{crit}$ is already strong (e.g., Fig. 15), because then the boost sets in very fast, resulting in dN/dE rising with energy at around E_{crit}. The rise is actually very sharp, but it is smoothed by the energy resolution of the instrument. An improvement in the energy resolution would increase the significance of the feature and improve the determination of E_{crit}. In contrast, if E_{crit} is in the range in which the EBL absorption is small or negligible (Fig. 14), the feature at E_{crit} would just be a flux drop of at most $\simeq 30\%$ [143], also washed out by the instrumental energy resolution. In those cases, though a high-energy boost may still be clearly detected, it would be hard to determine the exact value of E_{crit}. This is because, in the formalism described in Ref. [143], similar ALP boost factors are always achieved at energies $E > E_{crit}$, independently of the particular value of E_{crit} in each case.

3.2. Prospects

For each of the E_{crit} values scanned, we have performed 10^3 simulations of a CTA observation, all with the same source flux and observation time. We consider that a given value of E_{crit} is within the reach of CTA whenever the median of the χ^2-probability distri-

Fig. 15. Same as in Fig. 14, but with $E_{crit} = 1$ TeV. Note that in scenarios like this, where E_{crit} is within the energy range in which the EBL absorption is already large, the *boost* in the flux shows up as a sudden rise (smeared out by the spectral resolution of the instrument) which would even allow to determine E_{crit} accurately.

bution is below 2.9×10^{-7}, which corresponds to 5 standard deviations. In Fig. 16 we show the median of the χ^2 probability versus E_{crit}, for two different assumptions on the source flux and two different observation times. The range of E_{crit} which can be probed with CTA for the different scenarios is the one for which the curves in Fig. 16 are below the dashed horizontal line. As expected, the range becomes larger as we increase the observation time and/or the flux of the source. A 0.5 h duration flare like the one reported in [149] would not be enough for CTA to detect a significant effect in any of the tested ALP scenarios, i.e., the solid black line never goes below the dashed line for any value of E_{crit}. A flare of similar intensity, but lasting 5 h (green line) would already be enough to see the boost due to ALPs for those scenarios with $E_{crit} \leqslant 500$ GeV. In Fig. 16 we can also see that for a hypothetical flare with an intensity 5 times larger, lasting 5 h, the accessible range of E_{crit} would extend up to 1.3 TeV.

4. High energy violation of lorentz invariance

Lorentz invariance (Li) lies at the heart of all of modern physics, in particular the unification of space and time through the principle of Special Relativity. Space–time was elegantly promoted to be a dynamic entity in the covariant classical theory of gravity namely General Relativity (GR) which has been rigorously tested on astronomical scales and underlies the mathematical description of cosmology. Similarly quantum mechanics has been successfully married with Special Relativity to yield the quantum theory of fields which underlies the very successful Standard Model of leptons and quarks and the gauged electromagnetic, weak and strong forces. However it has proved considerably more difficult to unify gravity with the other forces, since GR is fundamentally non-renormalisable. A fully quantum theory of gravity (QG) is still beyond our grasp although there has been significant progress towards this goal in various approaches such as superstring theory and loop quantum gravity [155]. QG should describe dynamics at the Planck energy $E_{Pl} = \sqrt{\hbar c/G_N} \simeq 1.22 \times 10^{19}$ GeV or equivalently the Planck length $l_{Pl} = \sqrt{\hbar G_N/c^3} \simeq 1.62 \times 10^{-33}$ cm, where gravitational effects should become as strong as the other forces and the notion of space–time is likely to need revision. This has opened up the possibility that Li may be violated by QG effects although, lacking a fully dynamical theory, the expectation is generic rather than definite. For example quantum fluctuations may produce

'space–time foam' at the Planck scale resulting in a non-trivial refractive index and anomalous dispersion of light *in vacuo*, i.e., an energy dependence of the speed of light. Hence over the past decade, there has been tremendous interest in testing Li at high energies as part of what has come to be called 'quantum gravity phenomenology' [156–158].

Possible energy dependence of the speed of light in the vacuum has been predicted, in the framework of several theories dealing with quantum gravity models and effective field theory models [159]. The seminal paper by Amelino-Camelia et al. [160] proposed that this can be parameterised by a Taylor expansion of the usual dispersion relation:

$$c^2 p^2 = E^2 \left[1 \pm \xi_1 (E/E_{Pl}) \pm \xi_2 (E/E_{Pl})^2 \pm \dots \right], \quad (3.1)$$

where the value of the co-efficients ξ_α would be specified by the theory of quantum gravity (and may well turn out to be zero). For example there are specific predictions in some toy models [161,162] and a general parameterisation can be provided in the framework of effective field theory [159]. For more details see the introduction by [163] in Part A of this Special Issue. Typically, two scenarios are envisaged according to whether the linear term or the quadratic term is dominant, parametrised by the scale parameters ξ_1 (linear case) and ξ_2 (quadratic case) respectively. The point is that while QG effects would be prominent only at the Planck scales, there would be residual Lorentz invariance violation (LIV) effects at lower energies (GeV–TeV) in the form of anomalous photon velocity dispersion.

Amelino-Camelia et al. [160] also noted that over a cosmological distance L, the magnitude of time-delay Δt induced by LIV between two photons with an energy difference ΔE is detectable:

$$\Delta t \simeq \left(\frac{\Delta E}{\xi_\alpha E_{Pl}} \right)^\alpha \frac{L}{c} \quad (3.2)$$

where $\alpha = 1$ or 2 according to whether the linear or quadratic terms dominates in Eq. (3.1). The energy scale of QG is commonly expected to lie somewhere within a factor ξ_α of E_P. The best limit on the linear term has recently been placed by Fermi-LAT observations of GeV photons from GRB 090510 ($z = 0.903$) which require $M_1 = E_{Pl}/\xi_1 > 1.5 \times 10^{19}$ GeV [164]. The most constraining limit on the quadratic term $M_2 = E_{Pl}/\xi_2 > 6.4 \times 10^{10}$ GeV come from observations of an exceptional flare of the active galactic nucleus (AGN) PKS 2155–304 with the H.E.S.S. telescope [165].

It is important to keep in mind that although the QG induced time-delay is proportional to energy (as opposed to conventional dispersion effects which vary as inverse power of energy) similar time-delay effects may be intrinsic to the source [166]. Therefore, in order to distinguish between source and propagation time-delays, different types of sources should be considered with different physical properties and situated at different cosmological distances. For such studies, AGN and Gamma-Ray Bursts (GRBs) are the best candidates to test Eq. (3.2). AGN cover the higher energies (up to few TeV) and lower redshift regime (probably up to $z \sim 0.8 - 1$) and GRBs the lower energies (probably few tens of GeV) but higher redshifts. Other promising candidates could be pulsars which until now have yielded constraints one order of magnitude weaker than the ones derived from AGN [167].

4.1. The consequences of improved sensitivity and larger energy coverage of CTA on time-delays recovery

Using the Maximum Likelihood Estimation method (MLE) of [168], we investigate the effects that the improved CTA performance, in terms of increased statistics and broader energy lever arm, have on the time-delay recovery.
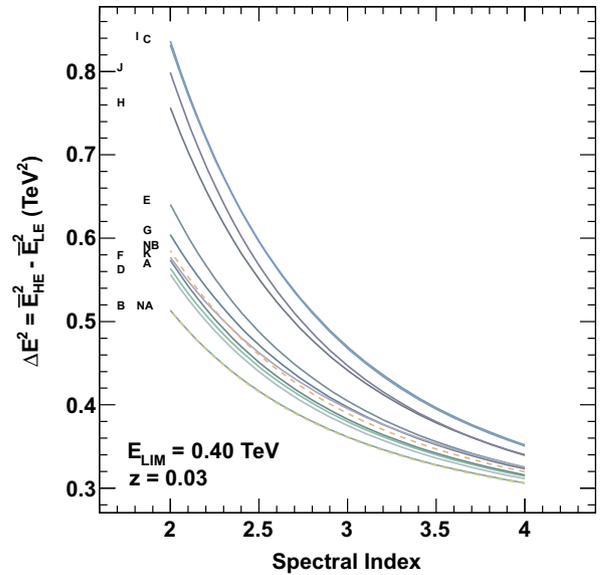
Fig. 17. Parameter ΔE^2 as a function of the spectral index for all arrays considered in CTA Monte Carlo simulations. The configurations have different layouts and number of telescopes. See details in the text.

Five hundred realisations of Gaussian-shaped "pulsed" light curves were generated for several values of time-delays between -60 s TeV^{-1} and $+60$ s TeV^{-1} in steps of 10 s TeV^{-1}. This allowed an estimate of the value of the error δt_r on the measured time-delay Δt_r. The error decreases as $N_\gamma^{-1/2}$, where N_γ is the number of photons included in the likelihood fit, and saturates at a value of about 3 s TeVs^{-1}, about a factor of 3 less than the current generation of IACTs, due to the increased statistics of CTA. The effect of the increase in the energy lever-arm, provided by the wide coverage of CTA from few tens of GeV to several tens of TeV, has also been addressed for the different array configurations taking into account the absorption of Extragalactic Background Light (EBL) using the model of [169],[6] and a spectral break at around 100 GeV. The photons are thus separated into two populations at "high" and "low" energies with average values marked as $\bar{E}_{HE}$ and $\bar{E}_{LE}$ respectively. Fig. 17 shows the variation of the energy lever-arm for different CTA configurations in energy-squared (quadratic case) $\Delta E^2 = \bar{E}_{HE}^2 - \bar{E}_{LE}^2$, after a convolution with the effective area and for a given choice of the energy value separating high and low energy bands $E_{LIM} = 400$ GeV. This value is almost stable regardless of the array or the spectral index [170]. The ranking shows that arrays I, C, J and H for the southern site and NB for the northern site are favourable for LIV studies.

The intrinsic variability of the photon emission by astrophysical sources such as GRBs and AGN is the main systematic uncertainty in LIV searches. Until now, the detected variability of the AGN was limited to about 100 s, partially due to the limited statistics of the data. The possibility of improved separation of the initially unresolved double peak structures was investigated with light curve simulations and time-delay reconstruction using again the MLE method. Fig. 18 shows the minimal peak separation which would allow distinguishing between two Gaussian spikes of the same standard deviation σ_G for different photon statistics: a H.E.S.S.-like measurement, a CTA-like measurement with an improved photon collection by a factor 100, and a more optimistic scenario with a factor 1000 more photons.

---

[6] This is a conservative choice – by using more transparent EBL models like that of [150], the results would be more promising.
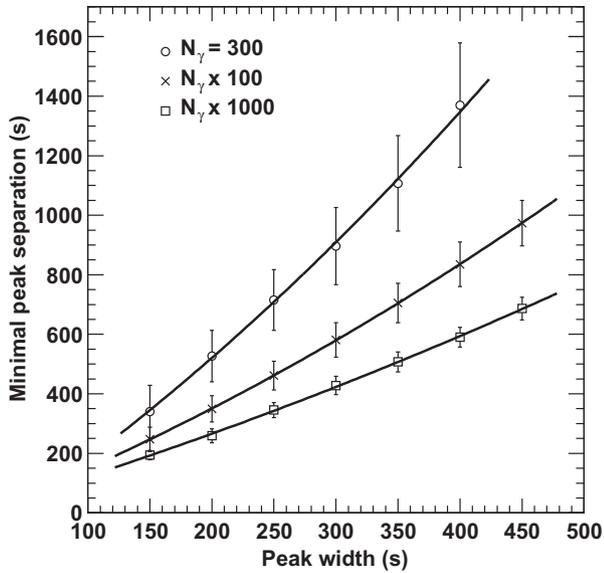
Fig. 18. Minimal distinguishable separation of two Gaussian peaks as a function of their width, in case of a H.E.S.S.-like measurement (open circles), a CTA-like measurement (crosses) and an ideal situtation where a ten times more photons than in the CTA measurement could be collected.

4.2. Sensitivity to TeV photons for selected benchmark AGN

Following the suggestion of Amelino-Camelia et al. [160] we define a sensitivity factor $\eta = |\Delta t_d|/T$, where Δt_d is the magnitude of the time-delay introduced into the flare and T is duration of the burst/flare feature that is being examined. In Refs. [171,172] it is shown that $\eta \geqslant 0.3$ is required to determine whether the observed flare time sequence has been skewed in comparison to its original form. To improve upon current limits will require observations of photons at energies larger than 10 TeV (for a given redshift) or observations of similar flares from much more distant AGN. In the following, we calculate the integral numbers of photons from representative AGN to test LIV signatures in AGN flares.

We have taken three VHE AGN representative of several known situations: an AGN-flare with high brightness (Mrk 421), an AGN-flare that shows short variability timescales (PKS 2155–304) and the AGN with the largest known redshift (3C 279) observed at VHE. The spectra in their highest recorded flux state have been taken from current IACT observations, extrapolated to higher energies, convolved with the performance curves of the various CTA array layouts and integrated assuming a flare duration lasting for the appropriate time such that $\eta = 0.3$. The results are shown in Fig. 19. Since this falls into the category of unbinned methodologies, the precision in the time resolution is the same as the time precision of each array (i.e., better than 1 μs). The uncertainty in the time-delay for a single photon is the time precision modulo of the energy resolution (being less than 10% as specified) and the distance (negligible), and saturates at 10 s TeVs^{-1} Gpcs^{-1}. This translates into a Planck scale effect of $\mathcal{O}(10)$ s (i.e., as good as a binned method would have for more than 100 photons).

Mrk 421 is known to show spectral hardening with increasing flux, and can have very hard spectra indeed on short timescales, as evidenced by Flare C in Ref. [173] – see discussion by Gaidos et al. [174]. For the redshift $z = 0.03$ of Mrk 421, Planck scale effects could be expected to induce a delay of ~ 1 s TeVs^{-1}; for $E \geqslant 10$ TeV photons this means we would need to be able to time resolve flare features at an unprecedented ~ 30 s duration. Whilst features this fast have yet to be identified, this could be because they are below the sensitivity of current instruments and the top panel of Fig. 19
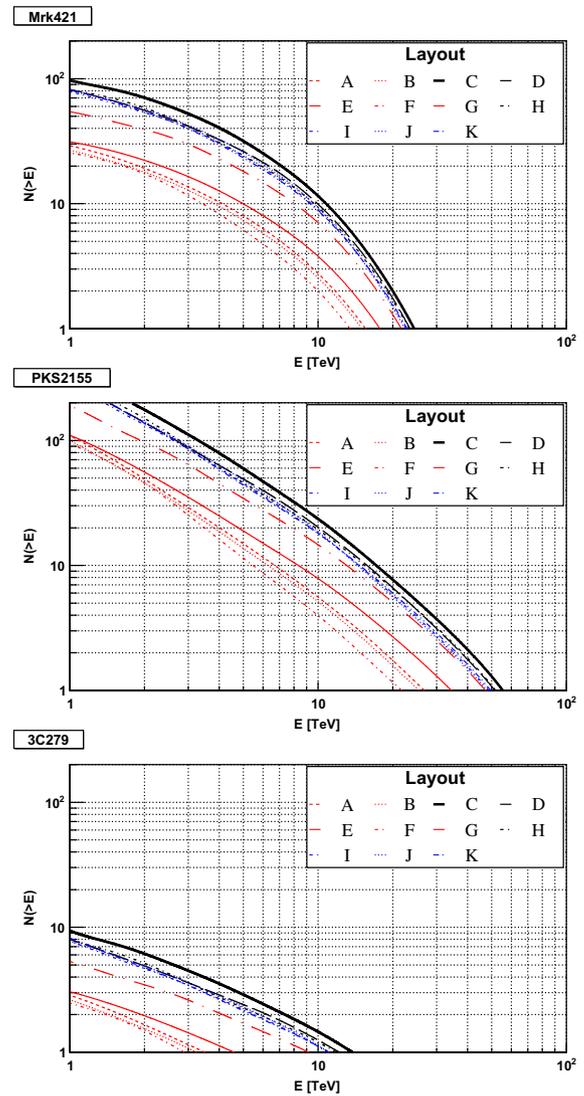
Fig. 19. Integral number of events above a given energy, expected for the various array configurations for simulated flares, for $N(> 10\,\mathrm{TeV}) = 10$ photons. Each panel is accumulated for the appropriate flare timescale required to be able to determine if Planck scale quantum gravity induced LIV is present. The top panel is for a 10 Crab Mrk 421 flare [173] if it lasted for 30 s duration; the middle panel is PKS 2155–304 similarly at its high level [175], but 120 s duration; the bottom panel is for a 610s 3C 279 flare at its highest recorded flux level [176].

demonstrates that, if present, such features can indeed be probed. For PKS 2155–304, the redshift $z = 0.117$ implies that CTA would need features on the timescale of 120 s to test Planck scale effects, which is still a factor of a few faster than the 240–610 s rising and falling timescales of the ~ 7 Crab flares observed to date [175] but, as shown in the middle panel of Fig. 19, we would easily have sufficient photons to resolve such features. For 3C 279 ($z = 0.536$, [176], even though the flare timescale of 610 s required for such a distant AGN are well within the variability timescales we currently observe for blazars, the photon flux we expect ($\sim 10\%$ Crab) from such a distant source is expected to be too low to resolve such features at the highest energies, because of the attenuation of the photon flux through interactions with the EBL.

Concerning the different CTA arrays, Fig. 19 shows that the best performing arrays at high energies are C, D, H, I, J, K. While it may be of more interest to find out if they would detect sufficient photons on which to perform tests for time-delay, we note that there are a number of unbinned methods that can cope with sparse

datasets (see, e.g., [171,165,177]) so that 10 photons of E (>=10 TeV) are required in order to be able to begin to test for LIV.

4.3. Time-delay recovery with realistic source lightcurve and spectra for the linear case

For this study, we produce 2500 pairs of lightcurves (with and without time-delays), following the method of [178] for each of the total 13 CTA arrays (11 Southern array $A \ldots K$ and 2 Northern arrays NA, NB), as shown in Fig. 20. We scan the space of possibilities by selecting random values in the 5-dimensional space characterised by the following parameters:

– time-delays in the range $\xi_1 = 0.1 - 5$ (linear case)
– AGN redshift linearly in the range $0.03 - 0.6$
– energy spectrum power law slope between 20 GeV and 20 TeV in the range $1 - 2.5$, and with a spectral cutoff at 120 GeV
– Flux level in the range $10^{-11} - 10^{-12}$ ph cm^{-2} ss^{-1}
– different observational periods: (a) single day observations consisting of 3 pointings of 30 and 15 min, (b) weekly observations consisting of 3 nightly pointings of 30 and 15 min, and (c) monthly observations consisting of 2 nightly pointings of 30 and 15 min.

The photons thus generated are then distributed as a function of time, based on the variability type that we have initially assumed (e.g., red-noise). These light curve pairs incorporate delay effects accumulated over a given distance depending on the ΔE of each pair. The light curve pairs are subsequently convolved with the CTA arrays performance, using the effective area, the background count rate and differential sensitivity. Finally, for each CTA array, we recover the observed time-delays using the cross-power spectral analysis method of [179]. For each pair of light curves and for each array we consider the *quality factor* between the simulated time-delay Δt_d and the recovered time-delay Δt_r defined as:

$$q = |\Delta t_d - \Delta t_r|/\delta t_r, \tag{3.3}$$

where δt_r is the width of the Gaussian distribution of the recovered time-delays coming from the simulations.
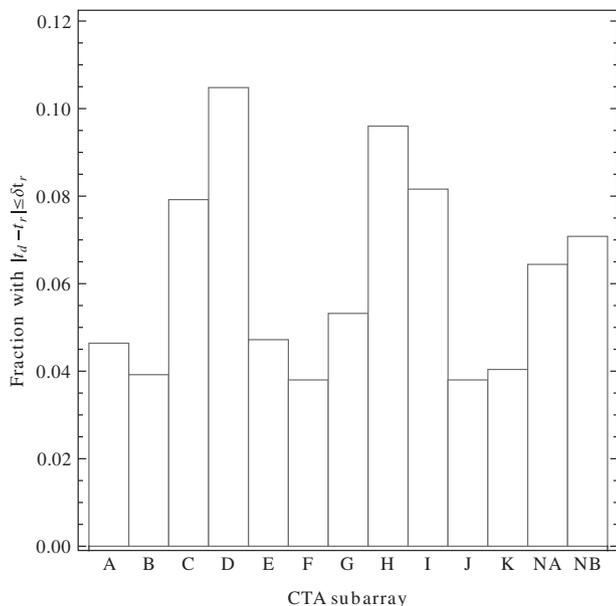
Fig. 20. Time-delay recovery fraction with quality factor $q < 1$ for each CTA configuration. See text for details.

When considering all the 13 arrays together, we find on average that 6% of the time-delays are recovered with $q < 1$. This is a very strict limit. If one relaxes this limit to $q < 2$ and $q < 3$, respectively 77% and 99% of the time-delays in our sample of events are recovered, thus making the prospects of detecting (or constraining) LIV signatures with CTA rather optimistic.

To understand which arrays have the best prospects, the time-delay recovery results for each array individually is shown in Fig. 20, adopting the limit of $q < 1$. From the plot we see that the best CTA configurations for time-delay recovery are C, D, H, I and NB respectively for the Southern and Northern hemispheres.

5. Other physics searches with CTA

In this section, we highlight topics of fundamental physics searches that were discussed in recent years and whose scenarios could be studied or hopefully constrained with CTA.

There are several caveats if one wants to present such various and complex topics "in a nutshell". First of all, the list of topics is not exhaustive; only a subset of topics is reported here. Second, some of the studies presented in this section may not be up-to-date by the time this article is published: theories in this area evolve and are updated exceedingly rapidly. In addition, most of these studies were formulated only within the context of the current generation of IACTs, and not for CTA. Whenever possible, considerations about the prospects for CTA will be addressed. Third, the discussion will mostly be of only a qualitative nature. The goal in this contribution is to provide an introductory discussion of the area, with the aim of encouraging others to explore in more detail these and other interesting new physics possibilities. Let us add that pursuing exotic physics with IACTs (and hence CTA) should be done because (a) it is possible (this may seem a naive argument, but, given the *terra incognita* offered by a new observatory such as CTA, it is a strong one); (b) VHE gamma rays have been identified as likely drivers of truly fundamental discovery. VHE gamma rays are a tool to explore new physics and new astrophysical scenarios, the nature of which may contain yet unknown, and unexpected, features. The potential for revolutionary discovery is enormous.

5.1. High energy tau-neutrino searches

Although optimized to detect electromagnetic air showers produced by cosmic gamma-rays, IACTs are also sensitive to hadronic showers. Inspired by calculations made by the AUGER collaboration and D. Fargion (see, e.g., [180–185]), the possible response of IACTs to showers initiated by very high energy τ-particles originating from a ν_τ collision with the sea or underneath rock is described.

It is well known that neutrinos of energies above the TeV energy range can form part of the cosmic rays hitting the Earth. The origin of such neutrinos could be from point-like sources like galactic microquasars [186,187] or extragalactic blazars [188,189] or gamma-ray bursts [190]. There are also diffuse fluxes of high energy neutrinos predicted to come from unresolved sources, including interactions of EHE cosmic rays during their propagation [191]. Finally, one could think of a more exotic origin of high energy neutrinos like those coming from DM particle annihilation, topological defects or cosmic strings [192–194]. Neutrinos are produced in astrophysical sources or during the transport, mainly after pion and subsequent muon decays:

$$\pi^+ \rightarrow \mu^+ \, \nu_\mu \qquad \mu^+ \rightarrow \bar{\nu}_\mu \, e^+ \, \nu_e \tag{4.1}$$
$$\pi^- \rightarrow \mu^- \, \bar{\nu}_\mu \qquad \mu^- \rightarrow \nu_\mu \, e^- \, \bar{\nu}_e \tag{4.2}$$

such that the typical neutrino family mixing at the source is $(\nu_e, \nu_\mu, \nu_\tau) = (1 : 2 : 0)$. Tau-neutrinos are found either at the source,

if charmed mesons are formed instead of pions, or are created during the propagation, after flavor mixing, such that at Earth, the neutrino family mixing could be $(\nu_e, \nu_\mu, \nu_\tau)_{\text{Earth}} = (1:1:1)$ [195].

The ν_τ channel has several advantages with respect to the electron or muon channel. First, the majority of the possible τ decay modes lead to an (observable) air shower or a combination of showers. Only 17.4% of the decays lead to a muon and neutrinos, considered to be unobservable for the effective areas of interest here. Moreover, the boosted τ lifetime ranges from some 50 m at 1 PeV to several tens of kilometers at EeV energies, almost unaffected by energy losses in matter and thus surpassing the muon range by a factor of ~20. Finally, the originating τ decays, instead of being absorbed by matter, and thus gives origin to another ν_τ of lower energy which in turn can produce a τ. At the highest energies, the Earth becomes completely opaque to all types of neutrinos giving rise to a pile-up of $\nu_\tau - \tau$.

To be able to observe atmospheric showers from ν_τ, the telescopes should be pointed at the direction where the τ escapes from the Earth crust after having crossed an optimized distance inside the Earth. Of course, this distance is strongly dependent on the telescope location, and no general conclusions can be drawn before the CTA site will be defined. In the past, two directions were proposed[7]: the observation slightly below the horizon downhill, e.g., if the telescope is located at a mountain, and the observation through a possible mountain chain in the vicinity (see Fig. 21). Both observations are at extremely low elevation angles, i.e., the telescopes pointing horizontally or even below the horizon, a fact that guarantees that the hadronic background diminishes until almost vanishing at the horizon. Only a small light contamination from continuous scattered star light and from scattered Cherenkov light by air showers will then be observed.

In Ref. [196], the effective area for ν_τ observation with the MAGIC telescope was calculated analytically. The results were the following: the maximum sensitivity would be in the range 100 TeV–1 EeV. For the observation downward towards the Sea, the sensitivity for diffuse neutrinos is very low because of the limited FOV (3 events/year/sr) and CTA cannot be competitive with other experiments like Icecube [197], Baikal [198], Auger [184], Antares [199] or KM3NeT. On the other hand, if flaring or disrupting point sources are observed, like is the case for GRBs, one can even expect an observable number of events from one GRB at reasonable distances, if the event occurs just inside a small observability band of about 1 degree width in zenith and an azimuth angle which allows to point the telescopes downhill.

For CTA, the situation could be different: taking an extension of the FOV of several times that of MAGIC in extended observation mode, the higher effective area and lower energy threshold, meaning higher fluxes, one naïve rescaling of the MAGIC calculations leads to relatively optimistic results, depending very much on the local geography. For point-like sources, the situation would not change so much w.r.t. the MAGIC case, unless the CTA telescopes are located close to a shielding mountain chain. The required observation times are still large, but one may argue that these observations can be performed each time when high clouds preclude the observation of gamma-ray sources.

5.2. Ultrarelativistic magnetic monopoles

The existence of magnetic monopoles is predicted by a wide class of extensions of the standard model of particle physics [200]. Considerable experimental effort has been undertaken during the last eight decades to detect magnetic monopoles. No confirmed success in detection has been reported at the present

---

[7] The study was made for the case of MAGIC [196].
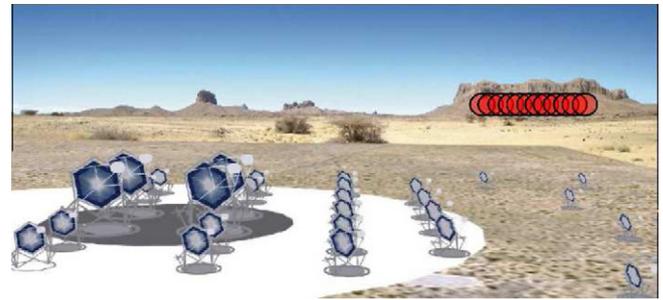
Fig. 21. Sketch of ν_τ searches with CTA. CTA telescopes can be pointed horizontally to a far mountain (if present) and observed the emerging τ-induced atmospheric shower.

time. Current flux limits on cosmogenic magnetic monopoles reach values of $\mathcal{O}(10^{-15}\ \text{cm}^{-2}\ \text{s}^{-1}\ \text{sr}^{-1})$ to $\mathcal{O}(10^{-17}\ \text{cm}^{-2}\ \text{s}^{-1}\ \text{sr}^{-1})$ depending on the monopole velocity. As outlined below, the CTA observatory is sensitive to a magnetic monopole flux.

According to [201] magnetic monopoles moving in air faster than the speed of light in air are emitting ≈ 4700 times more Cherenkov photons than an electric charge under the same circumstances. Being fast enough (Lorentz factor $\gamma > 10^3$) and heavy enough (mass $Mc^2 > 1\text{TeV}$) magnetic monopoles that possibly propagate through the earth atmosphere are neither significantly deflected by the Earth's magnetic field nor loose a significant amount of energy through ionization [202]. Assuming the last two constraints to be fulfilled a magnetic monopole moving through the Earth's atmosphere propagates on a straight line, thereby emitting a large amount of Cherenkov photons. This process of a uniform emission of intensive Cherenkov light differs from the Cherenkov light emitted by secondary particles in a shower initiated from a high energy cosmic or gamma-ray. As shown by [202], the number of triggered pixels in a telescope array is typically smaller and the intensity of the triggered pixels is typically higher for magnetic monopoles compared to events originating from cosmic or gamma-rays. Cuts in a parameter space spanned by the number of triggered pixels in the CTA array and the number of pixel with high intensity allow for an excellent discrimination between magnetic monopole events and background from cosmic or gamma-rays. The effective detection area of H.E.S.S. [203] for magnetic monopoles has been studied in detail [202]. Extrapolating the results of this study for CTA with its one order of magnitude increased design collection area, leads to a typical CTA magnetic monopole effective area of $4500\text{m}^2\text{sr}$. In Fig. 22, we show that assuming around 3000 h of CTA data from different observations accumulated in about 4 years of array operation, the sensitivity of CTA to magnetic monopoles with velocities close to the speed of light can reach the Parker limit [200] of $\mathcal{O}(10^{-15}\ \text{cm}^{-2}\ \text{s}^{-1}\ \text{sr}^{-1})$. Despite being still two orders of magnitude worse than current monopole flux limits from neutrino experiments [204] this sensitivity will allow a technically independent and new test for the existence of magnetic monopoles.

5.3. Gravitational waves

The period of operation of CTA should hopefully see the detection of the first gravitational wave (GW) by ground-based interferometers, now in the "advanced sensitivity" design phase. The 3 km–scale Michelson interferometers Enhanced LIGO and Advanced Virgo [205] are increasing their sensitivity and extending the horizon distance of detectable sources up to hundreds of Mpc, depending on the frequency. Two additional smaller interferometric detectors are part of the network of GW observatories, the Japanese TAMA (300 m arms) and the German-British 600 m
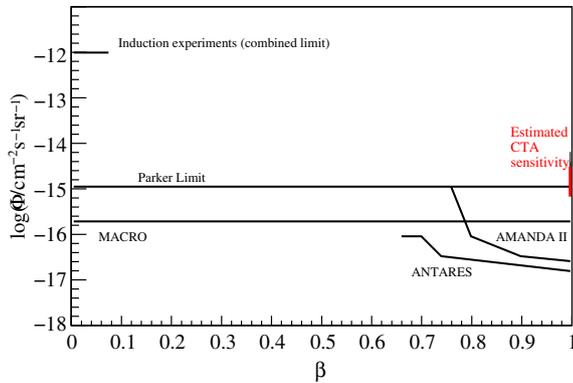
Fig. 22. Upper limits on the magnetic monopole flux as function of the monopole velocity inferred from different experiments [200,204] together with the estimated sensitivity of CTA. The sensitivity range shown for CTA indicates the dependence of the sensitivity on CTA design parameters and analysis details.

interferometer GEO600. The LIGO and Virgo observatories should start full operation in the advanced version in 2014/2015 and may operate together to fully reconstruct the arrival direction of a signal. They may localize strong GW bursts with an angular uncertainty down to one degree, while weaker signal have larger uncertainties, up to tens of degrees [206]. At the stage of conceptual design, the Einstein Telescope aims at increasing the arm length to 10 km, with three arms in a triangular pattern, implementing consolidated technology. It is foreseen to be located underground to reduce the seismic motion thus allowing a better sensitivity up to a factor 10 [207].

The most promising astrophysical mechanisms able to produce observable GWs are in–spiral and coalescence of binary compact objects (neutron stars and black holes), occurring for example during the merger of compact binary systems, as progenitors of supernova or neutron-star collapse, and associated with pulsar glitches. Signals from these systems may last from milliseconds to a few tens of seconds, but their expected rate and strength are uncertain [for a review, see, e.g., [208]]. Moreover, unexpected or unknown classes of sources and transient phenomena may be responsible for GW emission and may actually provide the first detection. Therefore combined GW and electromagnetic observations would be critical in establishing the nature of the first GW detection. While electromagnetic counterparts cannot be guaranteed for all GW transients, they may be expected for some of them [209,210] from radio waves to gamma-rays, such as in gamma ray bursts [211], ultra high-luminous X-ray transients and soft gamma repeater [212]. Electromagnetic identification of a GW would confirm the GW detection and improve the reconstruction and modeling of the physical mechanism producing the event. Moreover, significant flaring episodes identified in the electromagnetic band could serve as an external trigger for GW signal identification, and could even be used to reconstruct independently the source position and time, thus allowing the signal-to-noise ratio required for a confident detection to be lowered. The feasibility of this approach has been corroborated through dedicated simulations by the LIGO and Virgo collaborations [213].

CTA has the capability to pursue such a program of immediate follow-up of target of opportunity alerts from GW observatories, and to interact with GW collaborations to pursue offline analysis on promising candidates. The capability of CTA to observe in pointed mode with small FOV or in extended mode covering many square degrees of sky, is unique to follow strong and weak GW alerts. The observation mode should resemble the GRB procedure, which allow a fast repositioning on the order of tens of seconds.

In the era in which ground-based gravitational wave detectors are approaching their advanced configuration, the simultaneous

operation of facilities like CTA and Virgo/LIGO may open, in the forthcoming years, a unique opportunity for this kind of multi-messenger search.

6. Summary and conclusion

In this study we have investigated the prospects for detection and characterization of several flavors of physics beyond the standard model with CTA.

6.1. Particle dark matter searches

We have investigated dark matter (DM) searches with CTA for different observational strategies: from dwarf satellite galaxies (dSphs) in Section 2.1, from clusters of galaxies in Section 2.4 and from the vicinity of the Galactic Centre in Section 2.8. In Section 2.11, we discussed spatial signatures of DM in the diffuse extragalactic gamma-ray background.

Concerning searches in dSphs of the Milky Way, we have investigated the prospects for detection of well-known "classical" dSph like Ursa Minor and Sculptor, and one of the most promising "ultra-faint" dSph, Segue 1 (Table 1.1). We have first shown that the predictions for core or cusp DM density profiles are quite similar for the baseline CTA angular resolution (Fig. 1). We have then simulated a 100 h observation for several CTA arrays, and found that for Segue 1, we can exclude velocity-averaged cross-sections $(\sigma_{ann}v)$ above $10^{-23} - 10^{-24}$ cm^3 s^{-1} depending on different annihilation channels (Fig. 2). We also presented the same results in terms of the minimum astrophysical factor for dSphs to be detected (Fig. 3), showing that astrophysical factors of at least 10^{21} GeV^2 cm^{-5} are needed. We finally showed the minimum intrinsic boost factor to achieve detection (Fig. 4), which for Segue 1 is about 25 for a hard annihilation spectrum. The best candidate arrays for dSph study are array *B* and *E*. Nevertheless, the robustness of our results is hindered by the yet not precise determination of the astrophysical factor in some cases. Forthcoming detailed astronomical measurements will provide clues for deep exposure observations on the most promising dSphs, with, e.g., the planned SkyMapper Southern Sky Survey [214], which will very likely provide the community with a new dSph population, complementing the Northern hemisphere population discovered by the SDSS. Also, the uncertainties on dark matter density will be significantly reduced by new measurements of individual stellar velocities available after the launch of the GAIA mission.[8] Stacking-methods of Fermi-LAT dSphs data were proven valid to make constraints more stringent [49,215,216]. The application of these methods for CTA is currently under study.

The search for DM signatures in galaxy clusters, investigated in Section 2.4 was performed for two representative clusters, Perseus and Fornax. The former one is thought to have the highest CR-induced photon yield, and the latter is thought to have the strongest DM-induced signatures. Compared to dSphs, the gamma-ray signatures of galaxy clusters have several contributions: in the first place, the DM signal is expected from an extended region that can be larger than a few degrees, and secondly, gamma-rays induced by interactions of accelerated cosmic rays with the ambient fields and/or by individual cluster galaxies are an irreducible background to the DM signal, as recently shown in Refs. [103,102]. We have simulated the prospects of detection in 100 h of observation by using MC simulations of extended sources. Regarding DM signatures, we have used the model of [30] for the Fornax cluster, and showed that in 100 h we could put contraints on the order of $(\sigma_{ann}v) < 10^{-25}$ cm^3 s^{-1} (Fig. 6), which are competitive with

---

respect to those obtained with dSphs. The results are promising: if the intrinsic boost factor from subhalos is larger than that predicted by the model we used, or mechanisms of Sommerfeld enhancement are at work, there is also the possibility to have a detection in $100 - 200$ h with array *B* or *E*. We have also considered the prospects of detection of CR-induced signal in hadronic acceleration scenarios in Fig. 5. We have seen that the CR-induced emission from the Perseus cluster could be detected in about 100 h. Finally, we discussed the more realistic case when DM– and CR-induced gamma-rays are treated together. We discuss that the difference in both the spatial and spectral features of the two emissions can be used as a method for discrimination, while more quantitative results need dedicated MC which were not available when writing this contribution. We underline that the extension of the expected DM emitting region in galaxy clusters represents a problem for current Cherenkov Telescopes since their FOV is limited to 3–5° and their sensitivity rapidly decreases moving away from the centre of the camera. CTA will overcome this limitation, having a FOV of up to 10° and an almost flat sensitivity up to several degrees from the centre of the camera. For galaxy cluster searches, CTA will hence mark the difference compared to the current generation of IACTs.

More promising are DM searches of annihilation signatures in the Galactic halo, where the DM density is expected to be known with much higher precision than in the Galactic Centre itself or in (ultra-faint) dSphs or galaxy clusters. This was studied in Section 2.8. By adopting dedicated observational strategies of the region close to the Galactic Centre, as shown in Fig. 8, it was shown that CTA has the potential to reach the thermal annihilation cross-section expected from WIMP DM of 10^{-26} cm^3 s^{-1} and lower (Fig. 9) in 100 h observation of the vicinities the Galactic Centre using the "Ring" method. Models with a large photon yield from DM annihilation will be constrained for even smaller cross-sections. It is also expected that the limits presented here can be improved by factor of a few when the stereoscopic analysis of CTA events has been understood so well that a further suppression of the background becomes feasible. This would be the first time that ground-based Cherenkov telescopes could reach this sensitivity level.

Besides observations of individual dedicated objects, the capabilities of CTA for searching DM signals in the diffuse background of gamma-ray radiation were discussed in Section 2.11. We discussed the reconstruction performance for different anisotropy power spectra and residual background level. Considering a current model for the anisotropy power spectra, we showed that CTA may be able to distinguish a DM-induced diffuse gamma-ray component from the astrophysical background.

In Fig. 23, we summarize the constraints that we expect with CTA for a WIMP annihilating purely into $b\bar{b}$ in 100 h observation, with the different targets discussed above. As already anticipated, the best results are expected for the observation of the vicinity of the Galactic Centre, where we expect to reach the thermal annihilation cross-section for WIMP DM of 10^{-26} cm^3 s^{-1}. Unlike present IACTs, whose sensitivity supersedes that of the Fermi-LAT at masses around a TeV, CTA will constitute the most sensitive instrument above masses of about 100 GeV. It should be noted that these estimates are conservative: the most important improvement can be expected from the possible redefinition and final optimization of the array layout.[9] In addition, the presented sensitivities were calculated using generic analysis which was not optimized specifically for the DM searches and thus our results could be considered conservative in this sense.

---

[9] For example, it is currently under disussion, the possibility to add 36 medium-size telescopes of Schwarzschild-Couder design to the arrays considered here. Preliminary simulations predict that improvement in the overall sensitivity by at least a factor of 2 compared to that studied here may be expected.
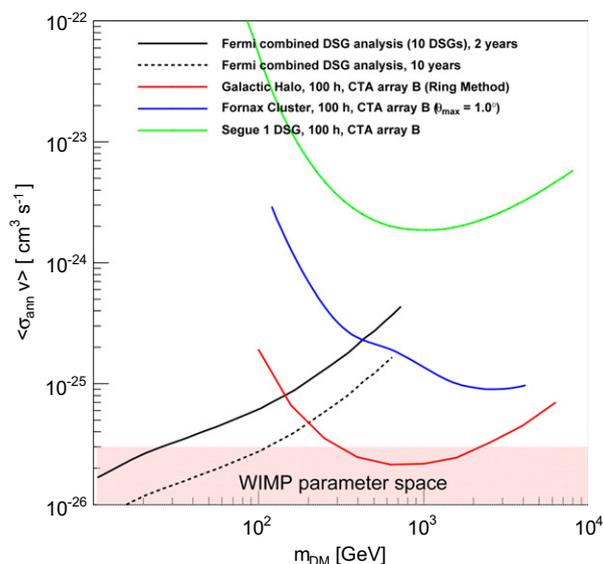
Fig. 23. Comparison of exclusion curves of Fermi-LAT in 24 months [52] and expected for 10 years (rescaled with the square root of time). The exclusion curves for the various targets studied in this contribution are also reported for the $b\bar{b}$ annihilation channel: for the dwarf satellite galaxy Segue 1 (green curve, see Section 2.1), for the Fornax galaxy cluster in case only DM-induced gamma-rays are considered (blue line, see Section 2.4) and and for the ring-method of observation of the Galactic Centre vicinities (red line, see Section 2.8). (For interpretation of the references to colour in this figure legend, the reader is referred to the web version of this article.)

Obviously, a firm *identification* of DM requires a very good spectral discrimination with respect to any possible astrophysical background. Spectral shapes and (even more so) absolute normalization of these backgrounds are often poorly determined and the DM signal most likely is small in comparison. As the extent to which these factors affect detection claims is highly model and target dependent, we refer to future detailed more focused assessments.

It has been shown that the detection of gamma-rays provides complementary information to other experimental probes of particle DM, especially that of direct detection, because CTA could be able to access a fraction of the parameter space not accessible otherwise [217,218]. With respect to particle searches at the LHC, the comparison is not straightforward, as LHC results are usually strongly related to specific models, and general conclusions are somewhat model dependent, as shown by recent publications from the ATLAS and CMS collaborations [219–221]. Generically, the discovery of a candidate for particle DM will be limited by the available centre-of-mass energy. Other scenarios exist, in the context of specific super-symmetric models for DM, that exhibit parts of the model space not accessible by the LHC [222]. In any case, LHC discovery of dark matter, would prompt the need for proof that the particle is actually consistent with the astrophysical DM, and close collaboration with LHC physicists is currently under organization to facilitate the optimal use of accelerator results within CTA. A concrete scenario has been analyzed by [223] in the case of a SUSY model in the so-called co-annihilation region. Simulated LHC data were used to derive constraints on the particle physics nature of the DM, with the result that the LHC alone is not able to reconstruct the neutralino composition. The situation improves if the information from a detection of gamma-rays after the observation of the Draco dSph by CTA is added to the game: in this case the internal degeneracies of the SUSY parameter space are broken and including CTA allows us to fully interpret the particle detected at the LHC as the cosmological DM. In the other case where the LHC will not detect any physics beyond the Standard Model, predictions were made in the context of the CMSSM [224] indicating that the

mass of the neutralino will be bound to be larger than approximately 250 GeV (400 GeV) if any new physics will be detected by the LHC for an energy of the centre-of-mass $\sqrt{s} = 14$ TeV and a luminosity of 1 fbs^{-1} (100 fbs^{-1}). In this scenario, CTA could be the only instrument to be able to detect and identify a WIMP candidate with masses beyond some hundreds GeV.

6.2. Axion-like particle searches

In Section 3, the prospect of searches for axion-like particle (ALP) signatures with CTA were studied. We saw that the theoretical photon/ALP mixing has important implications for astronomical observations, in such that the mixing could distort the spectra of gamma-ray sources, such as Active Galactic Nuclei (AGN) (or galactic sources), in the TeV range. This distortion adds to that caused by the absorption of the gamma-ray photons with UV and IR photons of the Extragalactic Background Light (see Fig. 13). The photon flux recently measured by some experiments, in particular at TeV energies, already exceeds that predicted by conventional models which attempt to explain spectra in terms of observed source spectra and/ or EBL density [144–148], one should not expect a photon flux as high as recently measured by some experiments, in particular at TeV energies. The hard spectrum deduced for some AGN is difficult to explain with conventional physics as well. While it is still possible to solve these puzzles without exotic physics, photon/ALP conversions may naturally alleviate both problems. In order to quantitatively study the effect of photon-axion conversion over cosmological distances, the total photon flux from a simulated flare of a far-distant source was considered. The source was simulated based on the flat spectrum radio quasar 4C + 21.35 (PKS 1222 + 21), $z = 0.432$, based on the observation performed by MAGIC [149], assuming an intrinsic unbroken power-law spectrum, and trying to understand the observability under different absolute flux normalization and flare duration (Figs. 14 and 15). The range of characteristic scale energy (critical energy, E_{crit}) described in Eq. (2.3), and thus the ALP mass that can be probed with CTA for the different ALP scenarios, is unknown and may be tested with CTA. In general, the distortion of the spectra due to ALP depends on the particular case, but as a general trend it will become larger as we increase the observation time and/or the flux of the source. As an example, we found that a 0.5 h duration flare like the one reported by MAGIC would not be enough for CTA to detect a significant effect in any of the tested ALP scenarios (Fig. 16). However, a flare of similar intensity, but lasting 5 h would already be enough to see the boost due to ALPs for those scenarios with $E_{crit} \leqslant 500$ GeV. For a hypothetical flare with an intensity 5 times larger, lasting 5 h, the accessible range of E_{crit} would extend up to 1.3 TeV (Fig. 16). Hopefully, not only PKS 1222 + 21 but also many other similar objects will be followed-up by CTA in the near future, making the field of ALP searches very promising.

We must emphasize that a boost in the flux is *only* possible in the energy range where the EBL is already at work. Thus, even for the most distant sources detected to date by IACTs, the energy range below ~100 GeV would not probably be of much help. On the other hand, even when E_{crit} lies within the energy range covered by IACTs, the drop/jump might not be accessible to these instruments. This would be the case, for instance, if E_{crit} is at the highest energies, from several to tens of TeV: the attenuation due to the EBL for a distant source would be huge, and the resulting flux, even after accounting for the ALP boost, too low to be detected by current IACTs or by CTA under any of the possible array configurations. Taking all these considerations into account, the most suitable energy for ALP searches with CTA seems to be an intermediate one in which the EBL is already present but still introduces only a moderate absorption, i.e., from a hundred GeV to a few TeV. As a result, we do not expect to obtain largely different results with candidate array configurations other than the one we used (array *E*), since they all perform very similarly in the intermediate energy range.

Finally, although very challenging given the uncertainty in the value of the IGMF, we should stress that the lack of detection of suspicious features in the spectra of distant gamma-ray sources might translate into useful constraints of the ALP parameter space (coupling constant and ALP mass). A more detailed study is definitely needed in order to find out what should be the best strategy to achieve the strongest constraints. This study will be done elsewhere.

6.3. Lorentz invariance violation

In scenarios where Lorentz invariance is violated by quantum gravitational effects, the space–time fabric may be distorted so that the vacuum shows a non-unitary refractive index and thus the light speed would be wavelength dependent. Observation of gamma-ray flares from far distant objects like active galactic nuclei or gamma-ray bursts, may allow to detect the time-delay between photons of different energies not caused by intrinsic source mechanisms. In Section 4, we discussed the sensitivity of the different CTA array configurations on detecting time-delays induced by Lorentz invariance violations (LIV). While limits on LIV from the current generation of IACTs are weaker than those estimated from Fermi-LAT measurement in the so-called linear case, CTA is likely to invert this scenario.

Using for the Maximum Likelihood Estimation method of [168], 500 Gaussian-shaped pulsed light-curves with time-delay from −60 s TeVs^{-1} to 60 s TeVs^{-1} were simulated and reconstructed with the different arrays. CTA will have improved statistics of photons and larger spectral lever-arm due to the enlarged energy range with respect to the current generation of IACTs. This will allow to better differentiate between the two Gaussian peaks as shown in Fig. 17 for the different arrays. This ability to differentiate peaks is also discussed in Fig. 18 for different width of the peaks. The best array configurations were discussed. As a result of these studies, a gain of about a factor 50 in the LIV scale for the "quadratic" model (see Eq. (3.1)) is expected, compared to current generation of telescopes, while the limits on the linear term will largely exceed the Planck energy scale.

We then used extrapolation to high-energies of real AGN spectra observed by the current generation of IACTs for three representative scenarios: a very bright AGN (Mrk 421), a fast-variable one (PKS 2155–304) and a high-redshift one (3C 279). High-energy photons above 10 TeV will guarantee the best sensitivity to observe LIV signatures, and CTA with its improved sensitivity at those high energies, will allow to collect sufficient photons, whereas photon statistics will always be the final limiting factor on tests for time-delay.

Finally, pairs of realistic AGN lightcurves with and without time-delay were simulated, and folded with CTA performance. For each array, we calculated the fraction of photons in which the time-delay was successfully measured according to a quality factor q (Eq. (3.3)). In the most stringent case ($q < 1$), we report the photon fraction recovery of each individual array in Fig. 20. As a main result, more than 10% of the time-delays can be recovered with several possible CTA arrays. If we relax the quality factor, and thus the precision on the reconstructed time-delay, essentially all the time-delays are recovered. We showed that arrays *C*, *D*, *H*, *I* and *NB*, respectively for the Southern and Northern hemisphere, have the best chance for detection.

Based on these genuinely different time-delay reconstruction methods we ensure that our final results, with respect to CTA-array ranking, are free from any possible systematic effects related to a given analysis method, e.g., idealized source redshift-distribution,

idealized source light-curves, and idealized source time-scales. In all analyses methods the sub-arrays *C*, *H*, *I* and *NB* seem to be sufficiently good to perform detection of LIV effects by measuring differences in the arrival times of VHE photons. That means that these arrays are in general sufficiently good to perform temporal studies of light-curve signals and even detection of time-delays in AGN induced intrinsically in the source. The latter is an interesting degeneracy, connected with the actual origin of the time-delays, that CTA will definitely be able to break through population studies not based on exceptional flaring states but on a routine basis.

6.4. Other searches

Finally, in Section 5, we have qualitatively discussed the physics case of a selection other exotic physic searches which are in principle possible with CTA: the observation of atmospheric showers from τ-particles emerging from the Earth crust, the observation of atmospheric showers from magnetic monopoles, and the possible follow-up of gravitational waves events. Despite the prospects being sometimes pessimistic, those subjects were shown to underline again the possibility of using an astronomical observatory such as CTA for fundamental physics searches.

As a final closing remark, we believe that CTA could offer one of the most powerful tools in the study of some of the most pressing questions in modern physics. In the next few years it may lead to a range of new observables, new methods and new theories. In preparation for these developments, it is essential that work such as that performed here is continued.

Acknowledgements

References

[1] M. Actis et al., Design concepts for the Cherenkov Telescope Array CTA: An advanced facility for ground-based high-energy gamma-ray astronomy, Exper. Astron. 32 (2011) 193–316.

[2] K. Bernloher et al., Monte carlo design patterns for the cherenkov telescope array, 2012. Astrop. Phys., this volume.

[3] E. Komatsu et al., Seven-Year Wilkinson Microwave Anisotropy Probe (WMAP) Observations: Cosmological Interpretation, Astrophys. J. Suppl. 192 (2011) 18.

[4] B.A. Reid, Applying the halo model to large scale structure measurements of the luminous red galaxies: SDSS DR7 preliminary results, Nucl. Phys. Proc. Suppl. 194 (2009) 129–132.

[5] V. Springel, J. Wang, M. Vogelsberger, A. Ludlow, A. Jenkins, A. Helmi, J.F. Navarro, C.S. Frenk, S.D.M. White, The Aquarius Project: the subhaloes of galactic haloes, Mon. Not. Roy. Astron. Soc. 391 (2008) 1685–1711.

[6] B. Anderson, M. Kuhlen, J. Diemand, R.P. Johnson, P. Madau, Fermi-LAT Sensitivity to Dark Matter Annihilation in Via Lactea II Substructure, Astrophys. J. 718 (2010) 899–904.

[7] V. Springel, S.D. White, C.S. Frenk, J.F. Navarro, A. Jenkins, et al., A blueprint for detecting supersymmetric dark matter in the Galactic halo, 2008. Preprint arXiv:0809.0894.

[8] W.H. Press, P. Schechter, Formation of galaxies and clusters of galaxies by self-similar gravitational condensation, Astrophys. J. 187 (1974) 425–438.

[9] R.K. Sheth, H. Mo, G. Tormen, Ellipsoidal collapse and an improved model for the number and spatial distribution of dark matter haloes, Mon. Not. Roy. Astron. Soc. 323 (2001) 1.

[10] V. Springel, S.D. White, A. Jenkins, C.S. Frenk, N. Yoshida, et al., galaxies and their large-scale distribution, Nature 435 (2005) 629–636.

[11] A.A. Klypin, A.V. Kravtsov, O. Valenzuela, F. Prada, Where are the missing galactic satellites?, Astrophys J. 522 (1999) 82–92.

[12] A.V. Kravtsov, Dark matter substructure and dwarf galactic satellites, Adv. Astron. 2010 (2010) 281913.

[13] R.K. de Naray, K. Spekkens, Do Baryons Alter the Halos of Low Surface Brightness Galaxies?, Astrophys J. 741 (2011) L29.

[14] M.G. Walker, J. Penarrubia, A Method for Measuring (Slopes of) the Mass Profiles of Dwarf Spheroidal Galaxies, Astrophys. J. 742 (2011) 20.

[15] M. Boylan-Kolchin, J.S. Bullock, M. Kaplinghat, Too big to fail? The puzzling darkness of massive Milky Way subhaloes, Mon. Not. Roy. Astron. Soc. 415 (2011) L40.

[16] M. Boylan-Kolchin, J.S. Bullock, M. Kaplinghat, The Milky Way's bright satellites as an apparent failure of LCDM, Mon. Not. Roy. Astron. Soc. 422 (2012) 1203–1218.

[17] G. Bertone, D. Hooper, J. Silk, Particle dark matter: Evidence candidates and constraints, Phys. Rept. 405 (2005) 279–390.

[18] J.L. Feng, Dark Matter Candidates from Particle Physics and Methods of Detection, Ann. Rev. Astron. Astrophys. 48 (2010) 495.

[19] G. Jungman, M. Kamionkowski, K. Griest, Supersymmetric dark matter, Phys. Rept. 267 (1996) 195–373.

[20] S.P. Martin, A Supersymmetry Primer, in: G.L. Kane (Ed.), Perspectives on Supersymmetry.

[21] M. Schmaltz, D. Tucker-Smith, Little Higgs review, Ann. Rev. Nucl. Part. Sci. 55 (2005) 229–270.

[22] G. Servant, T.M.P. Tait, Is the lightest Kaluza-Klein particle a viable dark matter candidate?, Nucl Phys. B 650 (2003) 391–419.

[23] S. Nussinov, Technocosmology: Could a technibaryon excess provide a natural missing mass candidate?, Phys Lett. B165 (1985) 55.

[24] R. Chivukula, T.P. Walker, Technicolor Cosmology, Nucl. Phys. B329 (1990) 445.

[25] S. Colafrancesco, S. Profumo, P. Ullio, Multi-frequency analysis of neutralino dark matter annihilations in the Coma cluster, Astron. Astrophys. 455 (2006) 21.

[26] J. Diemand et al., Clumps and streams in the local dark matter distribution, Nature 454 (2008) 735–738.

[27] L. Pieri, M. Lattanzi, J. Silk, Constraining the sommerfeld enhancement with cherenkov telescope observations of dwarf galaxies, MNRAS 399 (2009) 2033.

[28] A. Abramowski et al., Astropart. Phys. 34 (2011) 608–616.

[29] M.A. Sanchez-Conde, M. Cannoni, F. Zandanel, M.E. Gomez, F. Prada, Dark matter searches with Cherenkov telescopes: nearby dwarf galaxies or local galaxy clusters?, 2011. Preprint arXiv:1104.3530.

[30] A. Pinzke, C. Pfrommer, L. Bergstrom, Prospects of detecting gamma-ray emission from galaxy clusters: cosmic rays and dark matter annihilations, Phys. Rev. D84 (2011) 123509.

[31] L. Gao, C. Frenk, A. Jenkins, V. Springel, S. White, Where will supersymmetric dark matter first be seen?, 2011. Preprint arXiv:1107.1916.

[32] A. Sommerfeld, Ann. Phys. (Leipzig) 403 (1931) 257.

[33] M. Lattanzi, J.I. Silk, Can the WIMP annihilation boost factor be boosted by the Sommerfeld enhancement?, Phys Rev. D79 (2009) 083523.

[34] F. Aharonian, Observations of the Sagittarius Dwarf galaxy by the H.E.S.S. experiment and search for a Dark Matter signal, Astropart. Phys. 29 (2008) 55–62.

[35] F. Aharonian, A search for a dark matter annihilation signal towards the Canis Major overdensity with H.E.S.S., Astrophys. J. 691 (2009) 175–181.

[36] J. Albert et al., Upper limit for gamma-ray emission above 140-GeV from the dwarf spheroidal galaxy Draco, Astrophys. J. 679 (2008) 428–431.

[37] E. Aliu et al., MAGIC upper limits on the VHE gamma-ray emission from the satellite galaxy Willman 1, Astrophys. J. 697 (2009) 1299–1304.

[38] J. Aleksic et al., Searches for Dark Matter annihilation signatures in the Segue 1 satellite galaxy with the MAGIC-I telescope, JCAP 1106 (2011) 035.

[39] V.A. Acciari et al., VERITAS Search for VHE Gamma-ray Emission from Dwarf Spheroidal Galaxies, Astrophys. J. 720 (2010) 1174–1180.

[40] E. Aliu et al., VERITAS Deep Observations of the Dwarf Spheroidal Galaxy Segue 1, 2012. Preprint arXiv: 1202.2144.

[41] M. Wood et al., A Search for Dark Matter Annihilation with the Whipple 10 m Telescope, Astrophys. J. 678 (2008) 594–605.

[42] A. Abramowski et al., Phys. Rev. Lett. 106 (2011) 161301–+.

[43] F. Aharonian, Very high energy gamma-ray observations of the galaxy clusters Abell 496 and Abell 85 with H.E.S.S., A&A 495 (2008) 27.

[44] F. Aharonian et al., Constraints on the multi-TeV particle population in the Coma galaxy cluster with HESS observations, A&A 502 (2009) 437–443.

[45] J. Aleksic et al., MAGIC gamma-ray telescope observation of the perseus cluster of galaxies: implications for cosmic rays, dark matter and NGC 1275, Astrophys. J. 710 (2010) 634–647.

[46] A. Acciari et al., VERITAS upper limit on the VHE emission from the radio galaxy NGC 1275, Astrophys. J. 706 (2009) L275–L280.

[47] J. Aleksic et al., Constraining cosmic rays and magnetic fields in the perseus galaxy cluster with TeV observations by the MAGIC telescopes, 2011, Astron. Astrophys. 541 (2012) A99.

[48] A. Abramowski et al., Search for Dark Matter Annihilation Signals from the Fornax Galaxy Cluster with H.E.S.S., 2012, Astrophys. J. 750 (2012) 123.

[49] A. Abdo et al., Observations of Milky Way Dwarf Spheroidal galaxies with the Fermi-LAT detector and constraints on Dark Matter models, Astrophys. J. 712 (2010) 147–158.

[50] K.N. Abazajian, P. Agrawal, Z. Chacko, C. Kilic, Conservative Constraints on Dark Matter from the Fermi-LAT Isotropic Diffuse Gamma-Ray Background Spectrum, JCAP 1011 (2010) 041.

[51] G. Hutsi, A. Hektor, M. Raidal, Implications of the Fermi-LAT diffuse gamma-ray measurements on annihilating or decaying Dark Matter, JCAP 1007 (2010) 008.

[52] M. Ackermann et al., Constraining dark matter models from a combined analysis of Milky Way satellites with the Fermi-LAT, 2011. ArXiv e-print:1108.3546.

[53] T. Bringmann, F. Calore, G. Vertongen, C. Weniger, On the Relevance of Sharp Gamma-Ray Features for Indirect Dark Matter Searches, Phys. Rev. D84 (2011) 103525.

[54] G. Spengler et al., Search for photon line signatures with H.E.S.S., in: Proceedings of the 32nd International Cosmic Ray Conference.

[55] A. Abdo, M. Ackermann, M. Ajello, W. Atwood, L. Baldini, et al., Fermi LAT Search for Photon Lines from 30 to 200 GeV and Dark Matter Implications, Phys. Rev. Lett. 104 (2010) 091302.

[56] S. Funk, J. Hinton, Comparison of Fermi-LAT and CTA in the region between 10–100 GeV, 2012. Astrop. Physics, this volume.

[57] T.P. Li, Y.Q. Ma, Analysis methods for results in gamma-ray astronomy, Astrophys. J. 272 (1983) 317–324.

[58] W.A. Rolke, A.M. Lopez, J. Conrad, Limits and confidence intervals in the presence of nuisance parameters, Nucl. Instrum. Meth. A551 (2005) 493–503.

[59] G.J. Feldman, R.D. Cousins, Unified approach to the classical statistical analysis of small signals, Phys. Rev. D 57 (1998) 3873–3889.

[60] A. Tasitsiomi, A.V. Olinto, Detectability of neutralino clumps via atmospheric Cherenkov telescopes, Phys. Rev. D 66 (2002) 083006–+.

[61] M. Cirelli, G. Corcella, A. Hektor, G. Hutsi, M. Kadastik, et al., PPPC 4 DM ID: A Poor Particle Physicist Cookbook for Dark Matter Indirect Detection, JCAP 1103 (2011) 051.

[62] J.A.R. Cembranos, A. de La Cruz-Dombriz, A. Dobado, R.A. Lineros, A.L. Maroto, Photon spectra from WIMP annihilation, Phys. Rev. D 83 (2011) 083507–+.

[63] N. Evans, F. Ferrer, S. Sarkar, A 'Baedecker' for the dark matter annihilation signal, Phys. Rev. D69 (2004) 123501.

[64] M. Mateo, Dwarf galaxies of the local group, Ann. Rev. Astron. Astrophys. 36 (1998) 435.

[65] J.D. Simon, M. Geha, The Kinematics of the Ultra-Faint Milky Way Satellites: Solving the Missing Satellite Problem, Astrophys. J. 670 (2007) 313–331.

[66] A. Charbonnier, C. Combet, M. Daniel, S. Funk, J.A. Hinton, D. Maurin, C. Power, J.I. Read, S. Sarkar, M.G. Walker, M.I. Wilkinson, Dark matter profiles and annihilation in dwarf spheroidal galaxies: prospectives for present and future γ-ray observatories – I. The classical dwarf spheroidal galaxies, MNRAS 418 (2011) 1526–1556.

[67] D.G. York et al., The Sloan Digital Sky Survey: Technical Summary, Astron. J. 120 (2000) 1579–1587.

[68] G. Battaglia, A. Helmi, E. Tolstoy, M. Irwin, V. Hill, P. Jablonka, The Kinematic Status and Mass Content of the Sculptor Dwarf Spheroidal Galaxy, Astrophys. J. 681 (2008) L13–L16.

[69] L.E. Strigari, S.M. Koushiappas, J.S. Bullock, M. Kaplinghat, J.D. Simon, M. Geha, B. Willman, The Most Dark-Matter-dominated Galaxies: Predicted Gamma-Ray Signals from the Faintest Milky Way Dwarfs, Astrophys. J. 678 (2008) 614–620.

[70] V. Belokurov et al., Hair and A Hero: A Quintet of New Milky Way Companions, Astrophys. J. 654 (2007) 897–906.

[71] M. Niederste-Ostholt, V. Belokurov, N.W. Evans, G. Gilmore, R.F.G. Wyse, J.E. Norris, The origin of Segue 1, Mon. Not. Roy. Astron. Soc. 398 (2009) 1771–1781.

[72] M. Geha et al., The Least Luminous Galaxy: Spectroscopy of the Milky Way Satellite Segue 1, Astrophys. J. 692 (2009) 1464–1475.

[73] M. Xiang-Gruess, Y. Lou, W.J. Duschl, Dark matter dominated dwarf disc galaxy Segue 1, Mon. Not. Roy. Astron. Soc. 400 (2009) L52–L56.

[74] J.D. Simon, M. Geha, Q.E. Minor, G.D. Martinez, E.N. Kirby, et al., A Complete Spectroscopic Survey of the Milky Way Satellite Segue 1: The Darkest Galaxy, Astrophys. J. (submitted) (2010).

[75] R. Essig, N. Sehgal, L.E. Strigari, Bounds on Cross-sections and Lifetimes for Dark Matter Annihilation and Decay into Charged Leptons from Gamma-ray Observations of Dwarf Galaxies, Phys. Rev. D80 (2009) 023506.

[76] G.D. Martinez, J.S. Bullock, M. Kaplinghat, L.E. Strigari, R. Trotta, Indirect Dark Matter Detection from Dwarf Satellites: Joint Expectations from Astrophysics and Supersymmetry, JCAP 0906 (2009) 014.

[77] M.G. Walker, M. Mateo, E.W. Olszewski, J. Penarrubia, N. Evans, et al., A Universal Mass Profile for Dwarf Spheroidal Galaxies, Astrophys. J. 704 (2009) 1274–1287.

[78] P. Salucci, M.I. Wilkinson, M.G. Walker, G.F. Gilmore, E.K. Grebel, A. Koch, C. Frigerio Martins, R.F.G. Wyse, Dwarf spheroidal galaxy kinematics and spiral galaxy scaling laws, MNRAS 420 (2012) 2034–2041.

[79] O. Valenzuela et al., Is there Evidence for Flat Cores in the Halos of Dwarf Galaxies?: The Case of NGC 3109 and NGC 6822, Astrophys. J. 657 (2007) 773–789.

[80] J.F. Navarro, C.S. Frenk, S.D. White, A Universal density profile from hierarchical clustering, Astrophys. J. 490 (1997) 493–508.

[81] J.F. Navarro, A. Ludlow, V. Springel, J. Wang, M. Vogelsberger, S.D.M. White, A. Jenkins, C.S. Frenk, A. Helmi, The diversity and similarity of simulated cold dark matter haloes, Mon. Not. Roy. Astron. Soc. 402 (2010) 21–34.

[82] B. Moore, Evidence against dissipationless dark matter from observations of galaxy haloes, Nature 370 (1994) 629.

[83] R.A. Flores, J.R. Primack, Observational and theoretical constraints on singular dark matter halos, Astrophys. J. 427 (1994) L1–4. Revised versio.

[84] W.J.G. de Blok, S.S. McGaugh, A. Bosma, V.C. Rubin, Mass Density Profiles of LSB Galaxies, Astrophys. J. 552 (2001) L23–l26.

[85] F.C. van den Bosch, R.A. Swaters, Dwarf galaxy rotation curves and the core problem of dark matter halos, Mon. Not. Roy. Astron. Soc. 325 (2001) 1017.

[86] W.J.G. de Blok, The Core-Cusp Problem, Adv. Astron. (2010).

[87] M. Walker, C. Combet, J. Hinton, D. Maurin, M. Wilkinson, Dark matter in the classical dwarf spheroidal galaxies: a robust constraint on the astrophysical factor for gamma-ray flux calculations, Astrophys. J. 733 (2011) L46.

[88] J.A.R. Cembranos, A. de La Cruz-Dombriz, A. Dobado, R.A. Lineros, A.L. Maroto, Photon spectra from WIMP annihilation, Phys. Rev. D 83 (2011) 083507–+.

[89] R. Essig, N. Sehgal, L.E. Strigari, M. Geha, J.D. Simon, Indirect Dark Matter Detection Limits from the Ultra-Faint Milky Way Satellite Segue 1, Phys. Rev. D82 (2010) 123503.

[90] L. Pieri, G. Bertone, E. Branchini, Dark Matter Annihilation in Substructures Revised, Mon. Not. Roy. Astron. Soc. 384 (2008) 1627.

[91] D. Nieto, V. Martinez, N. Mirabal, J. Barrio, K. Satalecka, et al., A search for possible dark matter subhalos as IACT targets in the First Fermi-LAT Source Catalog, 2011. Preprint arXiv: 1110.4744.

[92] G. Voit, Tracing cosmic evolution with clusters of galaxies, Rev. Mod. Phys. 77 (2005) 207–258.

[93] P. Blasi, S. Gabici, G. Brunetti, Gamma rays from clusters of galaxies, Int. J. Mod. Phys. A22 (2007) 681–706.

[94] T.E. Jeltema, J. Kehayias, S. Profumo, Gamma Rays from Clusters and Groups of Galaxies: Cosmic Rays versus Dark Matter, Phys. Rev. D80 (2009) 023005.

[95] A. Pinzke, C. Pfrommer, Simulating the gamma-ray emission from galaxy clusters: a universal cosmic ray spectrum and spatial distribution, 2010, Mon. Not. Roy. Astron. Soc. 409 (2010) 449–480.

[96] M. Ackermann et al., Constraints on Dark Matter Annihilation in Clusters of Galaxies with the Fermi Large Area Telescope, JCAP 1005 (2010) 025.

[97] A.J. Cuesta et al., Dark Matter Decay and Annihilation in the Local Universe: Clues from Fermi, Astrophys. J. 726 (2011) L6.

[98] S. Zimmer, J. Conrad, f. t. F.-L. Collaboration, A. Pinzke, A Combined Analysis of Clusters of Galaxies – Gamma Ray Emission from Cosmic Rays and Dark Matter, 2011. Preprint arXiv:1110.6863.

[99] X. Huang, G. Vertongen, C. Weniger, Galaxy Clusters and Gamma-Ray Lines: Probing Gravitino Dark Matter with the Fermi LAT, 2011. Preprint arXiv:1110.6236.

[100] J. Han, C.S. Frenk, V.R. Eke, L. Gao, S.D. White, Evidence for extended gamma-ray emission from galaxy clusters, 2012. Preprint arXiv:1201.1003.

[101] T. Bringmann, Particle Models and the Small-Scale Structure of Dark Matter, New J. Phys. 11 (2009) 105027.

[102] J. Aleksíc et al., Discovery of very high energy gamma ray emission from NGC 1275 by the MAGIC telescopes, Astron. Astrophys., in press.

[103] J. Aleksic et al., Detection of very high energy gamma-ray emission from the Perseus cluster head-tail galaxy IC 310 by the MAGIC telescopes, 2010. ArXiv e-print:1009.2155.

[104] P. Blasi, S. Colafrancesco, Cosmic rays, radio halos and non-thermal x-ray emission in clusters of galaxies, Astropart. Phys. 12 (1999) 169–183.

[105] F. Miniati, Numerical modeling of gamma radiation from galaxy clusters, Mon. Not. Roy. Astron. Soc. 342 (2003) 1009.

[106] C. Pfrommer, T.A. Ensslin, V. Springel, Simulating cosmic rays in clusters of galaxies – II.A unified model for radio halos and relics with predictions of the gamma-ray emission, MNRAS 385 (2007) 1211–1241.

[107] T.A. Ensslin, C. Pfrommer, F. Miniati, K. Subramanian, Cosmic ray transport in galaxy clusters: implications for radio halos, gamma-ray signatures, and cool core heating, 2010. Preprint arXiv:1008.4717.

[108] S. Colafrancesco, P. Blasi, Clusters of galaxies and the diffuse gamma-ray background, Astropart. Phys. 9 (1998) 227–246.

[109] S. Colafrancesco, R. Lieu, P. Marchegiani, M. Pato, L. Pieri, On the DM interpretation of the origin of non-thermal phenomena in galaxy clusters, Astron. Astrophys. 527 (2011) A80.

[110] O.Y. Gnedin, A.V. Kravtsov, A.A. Klypin, D. Nagai, Response of dark matter halos to condensation of baryons: Cosmological simulations and improved adiabatic contraction model, Astrophys. J. 616 (2004) 16–26.

[111] S. Ando, D. Nagai, Fermi-LAT constraints on dark matter annihilation cross section with the Fornax cluster, 2012. Preprint arXiv:1201.0753.

[112] T. Bringmann, M. Doro, M. Fornasa, Dark Matter signals from Draco and Willman 1: Prospects for MAGIC II and CTA, JCAP 0901 (2009) 016.

[113] T. Bringmann, L. Bergstrom, J. Edsjo, New Gamma-Ray Contributions to Supersymmetric Dark Matter Annihilation, JHEP 01 (2008) 049.

[114] P. Gondolo, J. Silk, Dark matter annihilation at the galactic center, Phys. Rev. Lett. 83 (1999) 1719–1722.

[115] V. Springel, S.D.M. White, C.S. Frenk, J.F. Navarro, A. Jenkins, M. Vogelsberger, J. Wang, A. Ludlow, A. Helmi, Prospects for detecting supersymmetric dark matter in the Galactic halo, Nature 456 (2008) 73–76.

[116] F. Acero et al., Localizing the VHE γ-ray source at the Galactic Centre, MNRAS 402 (2010) 1877–1882.

[117] F. Aharonian et al., Spectrum and variability of the Galactic center VHE γ-ray source HESS J1745-290, AP 503 (2009) 817–825.

[118] F. Aharonian et al., Discovery of very-high-energy γ-rays from the Galactic Centre ridge, Nature 439 (2006) 695–698.

[119] Q.D. Wang, F.J. Lu, E.V. Gotthelf, G359.95-0.04: an energetic pulsar candidate near Sgr A∗, MNRAS 367 (2006) 937–944.

[120] F. Aharonian et al., HESS Observations of the Galactic Center Region and Their Possible Dark Matter Interpretation, Phys. Rev. Lett. 97 (2006) 221102–+.

[121] U. Schwanke, Dark matter searches with imaging atmospheric Cherenkov telescopes and prospects for detection of the Milky Way halo, in: 5th Patras Workshop on Axions, WIMPs and WISPS, 5th Patras Workshop on Axions, WIMPs and WISPS, pp. 120–122.

[122] J. Diemand, M. Kuhlen, P. Madau, M. Zemp, B. Moore, D. Potter, J. Stadel, Clumps and streams in the local dark matter distribution, Nature 454 (2008) 735–738.

[123] S. Ando, E. Komatsu, T. Narumoto, T. Totani, Dark matter annihilation or unresolved astrophysical sources? Anisotropy probe of the origin of the cosmic gamma-ray background, Phys. Rev. D 75 (2007) 063519.

[124] S. Ando, Gamma-ray background anisotropy from Galactic dark matter substructure, Phys. Rev. D 80 (2009) 023520.

[125] A. Couco, J. Brandbyge, S. Hannestad, T. Haugboelle, G. Miele, Angular signatures of annihilating dark matter in the cosmic gamma-ray background, Phys. Rev. D 77 (2008) 123518.

[126] J.M. Siegal-Gaskins, Revealing dark matter substructure with anisotropies in the diffuse gamma-ray background, J. Cosmol. Astropart. Phys. 10 (2008) 40–+.

[127] J. Siegal-Gaskins, Fermi-LAT Collaboration, E. Komatsu, Anisotropies in the diffuse gamma-ray background measured by the Fermi-LAT, 2010. In: Proceedings of Identification of Dark Matter 2010 (IDM 2010).

[128] A.A. Abdo et al., Spectrum of the isotropic diffuse gamma-ray emission derived from first-year fermi large area telescope data, Phys. Rev. Lett. 104 (2010) 101101.

[129] A.A. Abdo et al., Constraints on cosmological dark matter annihilation from the fermi-lat isotropic diffuse gamma-ray measurement, J. Cosmol. Astropart. Phys. 04 (2010) 014.

[130] R.D. Peccei, H.R. Quinn, CP conservation in the presence of pseudoparticles, Phys. Rev. Lett. 38 (1977) 1440–1443.

[131] D.A. Dicus, E.W. Kolb, V.L. Teplitz, R.V. Wagoner, Astrophysical bounds on the masses of axions and Higgs particles, Phys. Rev. D 18 (1978) 1829–1834.

[132] P. Sikivie, Experimental tests of the 'invisible' axion, Phys. Rev. Lett. 51 (1983) 1415–1417.

[133] S. Andriamonje et al., An improved limit on the axion photon coupling from the CAST experiment, JCAP 4 (2007) 10–+.

[134] E. Arik et al., Probing eV-scale axions with CAST, JCAP 0902 (2009) 008.

[135] S. Aune et al., CAST search for sub-eV mass solar axions with 3He buffer gas, 2011. ArXiv e-print:1106.3919.

[136] F.J. Iguaz, for the CAST Collaboration, The CAST experiment: status and perspectives, ArXiv e-prints (2011).

[137] L.D. Duffy et al., High resolution search for dark-matter axions, Phys. Rev. D 74 (2006) 012006–+.

[138] D. Hooper, P.D. Serpico, Detecting Axion-like Particles with Gamma Ray Telescopes, Phys. Rev. Lett. 99 (2007) 231102–+.

[139] A. de Angelis, M. Roncadelli, O. Mansutti, Evidence for a new light spin-zero boson from cosmological gamma-ray propagation?, Phys Rev. D 76 (2007) 121301.

[140] K.A. Hochmuth, G. Sigl, Effects of axion-photon mixing on gamma-ray spectra from magnetized astrophysical sources, Phys. Rev. D 76 (2007) 123011–+.

[141] M. Simet, D. Hooper, P.D. Serpico, Milky Way as a kiloparsec-scale axionscope, Phys. Rev. D 77 (2008) 063001–+.

[142] A. Mirizzi, G.G. Raffelt, P.D. Serpico, Signatures of axionlike particles in the spectra of TeV gamma-ray sources, Phys. Rev. D 76 (2007) 023001–+.

[143] M.A. Sánchez-Conde, D. Paneque, E. Bloom, F. Prada, A. Domínguez, Hints of the existence of axionlike particles from the gamma-ray spectra of cosmological sources, Phys. Rev. D 79 (2009) 123511–+.

[144] J. Aleksić et al., Observations of the Blazar 3C 66A with the Magic Telescopes in Stereoscopic Mode, Astrophys. J. 726 (2011) 58–+.

[145] E. Aliu et al., Discovery of a Very High Energy Gamma-Ray Signal from the 3C 66A/B Region, Astrophys. J. 692 (2009) L29–L33.

[146] Y.I. Neshpor, A.A. Stepanyan, O.P. Kalekin, V.P. Fomin, N.N. Chalenko, V.G. Shitov, Blazar 3C 66A: Another extragalactic source of ultra-high-energy gamma-ray photons, Astron. Lett. 24 (1998) 134–138.

[147] A.A. Stepanyan et al., Observations of the Flux of Very-High-Energy Gamma Rays from the Blazar 3C 66A, Astron. Rep. 46 (2002) 634–638.

[148] F. Krennrich, E. Dwek, A. Imran, Constraints on Energy Spectra of Blazars based on Recent EBL Limits from Galaxy Counts, Astrophys. J. 689 (2008) L93–L96.

[149] J. Aleksić et al., MAGIC Discovery of Very High Energy Emission from the FSRQ PKS 1222+21, Astrophys. J. 730 (2011) L8+.

[150] A. Domínguez et al., Extragalactic background light inferred from AEGIS galaxy-SED-type fractions, MNRAS 410 (2011) 2556–2578.

[151] Y.T. Tanaka et al., Astrophys. J. 733 (2011) 19–+.

[152] A. de Angelis, M. Persic, M. Roncadelli, Constraints on Large-Scale Magnetic Fields from the Auger Results, Mod. Phys. Lett. A 23 (2008) 315–317.

[153] A. Neronov, I. Vovk, Evidence for Strong Extragalactic Magnetic Fields from Fermi Observations of TeV Blazars, Science 328 (2010) 73.

[154] F. Tavecchio, G. Ghisellini, L. Foschini, G. Bonnoli, G. Ghirlanda, P. Coppi, The intergalactic magnetic field constrained by Fermi/Large Area Telescope observations of the TeV blazar 1ES0229+200, MNRAS 406 (2010) L70–L74.

[155] C. Rovelli, Notes for a brief history of quantum gravity, 2000, in: Presented at the 9th Marcel Grossmann Meeting in Roma, July 2000. E-print arXiv:gr-qc/0006061.

[156] S. Sarkar, Possible astrophysical probes of quantum gravity, Mod. Phys. Lett. A17 (2002) 1025–1036.

[157] D. Mattingly, Modern tests of Lorentz invariance, Liv. Rev. Relat. 8 (2005) 5–+.

[158] S. Liberati, L. Maccione, Lorentz Violation: Motivation and New Constraints, Ann. Rev. Nucl. Part. Sci. 59 (2009) 245–267.

[159] R.C. Myers, M. Pospelov, Ultraviolet Modifications of Dispersion Relations in Effective Field Theory, Phys. Rev. Lett. 90 (2003) 211601–+.

[160] G. Amelino-Camelia, J. Ellis, N.E. Mavromatos, D.V. Nanopoulos, S. Sarkar, Tests of quantum gravity from observations of γ-ray bursts, Nature 395 (1998) 525–+.

[161] J. Alfaro, H.A. Morales-Técotl, L.F. Urrutia, Loop quantum gravity and light propagation, Phys. Rev. D 65 (2002) 103509–+.

[162] J. Ellis, N.E. Mavromatos, D.V. Nanopoulos, Derivation of a vacuum refractive index in a stringy space time foam model, Phys. Lett. B 665 (2008) 412–417.

[163] J. Ellis, N.E. Mavromatos, Probes of Lorentz Violation, 2011. Astrop. Physics, this volume. Preprint arXiv:1111.1178.

[164] A.A. Abdo et al., A limit on the variation of the speed of light arising from quantum gravity effects, Nature 462 (2009) 331–334.

[165] A. Abramowski et al., Search for Lorentz Invariance breaking with a likelihood fit of the PKS 2155-304 Flare Data Taken on MJD 53944, Astropart. Phys. 34 (2011) 738–747.

[166] A. Mastichiadis, K. Moraitis, On the rapid TeV flaring activity of Markarian 501, A&A 491 (2008) L37–L40.

[167] A.N. Otte, Prospects of performing Lorentz invariance tests with VHE emission from pulsars, in: Proceedings of the 32nd International Cosmic Ray Conference.

[168] M. Martínez, M. Errando, A new approach to study energy-dependent arrival delays on photons from astrophysical sources, Astropart. Phys. 31 (2009) 226–232.

[169] T.M. Kneiske, K. Mannheim, D.H. Hartmann, Implications of cosmological gamma-ray absorption. I. Evolution of the metagalactic radiation field, A&A 386 (2002) 1–11.

[170] J. Bolmont, D. Emmanoulopoulos, A. Jacholkowska, J.P. Tavernet, Search for Lorentz Invariance Violation with flaring Active Galactic Nuclei: a prospect for the CTA, in: Proceedings of the 32nd International Cosmic Ray Conference. Http://galprop.stanford.edu/elibrary/icrc/2011/papers.html#0 883.

[171] U. Barres de Almeida, M.K. Daniel, A simple method to test for energy-dependent dispersion in high energy lightcurves of astrophysical sources, Astropart. Phys. 35 (2012) 850–860.

[172] U. Barres de Almeida, Physics from Time Variability of the VHE Blazar PKS 2155-304, Ph.D. thesis, Durham University, 2010. Ph.D. Thesis available at http://etheses.dur.ac.uk/593/.

[173] V.A. Acciari et al., TeV and Multi-wavelength Observations of Mrk 421 in 2006-2008, Astrophys. J. 738 (2011) 25.

[174] J. Gaidos, C. Akerlof, S. Biller, P. Boyle, A. Breslin, et al., Very Rapid and Energetic Bursts of TeV Photons from the Active Galaxy Markarian 421, Nature 383 (1996) 319–320.

[175] F. Aharonian et al., An exceptional very high energy gamma-ray flare of PKS 2155-304, Astrophys. J. 664 (2007) L71–L74.

[176] J. Aleksić et al., MAGIC Observations and multiwavelength properties of the quasar 3C 279 in 2007 and 2009, A&A 530 (2011) A4+.

[177] J.D. Scargle, J.P. Norris, J.T. Bonnell, An Algorithm for Detecting Quantum Gravity Photon Dispersion in Gamma-Ray Bursts: DisCan, Astrophys. J. 673 (2008) 972–980.

[178] J. Timmer, M. Koenig, On generating power law noise, A&A 300 (1995) 707–+.

[179] M.A. Nowak, B.A. Vaughan, J. Wilms, J.B. Dove, M.C. Begelman, Rossi X-Ray Timing Explorer Observation of Cygnus X-1. II. Timing Analysis, Astrophys. J. 510 (1999) 874–891.

[180] D. Fargion, Horizontal Tau air showers from mountains in deep vally: Traces of Ultrahigh neutrino tau, in: International Cosmic Ray Conference, volume 2 of International Cosmic Ray Conference, pp. 396–+.

semester